RECENT DEVELOPMENTS IN ASTROPHYSICAL AND COSMOLOGICAL EXPLOITATION OF MICROWAVE SURVEYS*

CARLO BURIGANA

INAF–IASF Bologna, Via Piero Gobetti 101, I–40129 Bologna, Italy †
Dipartimento di Fisica e Scienze della Terra, Università degli Studi di Ferrara, Via Giuseppe Saragat 1, I–44122 Ferrara, Italy
burigana@iasfbo.inaf.it

RODNEY D. DAVIES

Jodrell Bank Centre for Astrophysics, Alan Turing Building, School of Physics and Astronomy, University of Manchester, Oxford Road, Manchester, M13 9PL, UK
rdd@jb.man.ac.uk

PAOLO DE BERNARDIS

Dipartimento di Fisica, Università La Sapienza, P. le A. Moro 2, I–00185 Roma, Italy
paolo.debernardis@roma1.infn.it

JACQUES DELABROUILLE

APC, AstroParticule et Cosmologie, Université Paris Diderot, CNRS/IN2P3, CEA/lrfu, Observatoire de Paris, Sorbonne Paris Cité, 10, rue Alice Domon et Léonie Duquet, 75205 Paris Cedex 13, France
delabrouille@apc.univ-paris7.fr

FRANCESCO DE PAOLIS

Dipartimento di Matematica e Fisica "Ennio De Giorgi", Università del Salento
INFN (Istituto Nazionale di Fisica Nucleare), Sezione di Lecce
Via Arnesano, CP 193, I–73100 Lecce, Italy
Francesco.DePaolis@le.infn.it

MARIAN DOUSPIS

IAS, bat 121, Université Paris-Sud 11, Orsay, F–91400, France
marian.douspis@ias.u-psud.fr

RISHI KHATRI

Max Planck Institut für Astrophysik, Karl-Schwarzschild-Str. 1, 85741, Garching, Germany
khatri@mpa-garching.mpg.de

GUO CHIN LIU

Department of Physics, Tamkang University, Tamsui District, New Taipei City, 251, Taiwan

*Based on talks presented at the Thirteenth Marcel Grossmann Meeting on General Relativity, Stockholm, July 2012.

†Istituto Nazionale di Astrofisica – Istituto di Astrofisica Spaziale e Fisica Cosmica di Bologna, Via Piero Gobetti 101, I–40129 Bologna, Italy

liugc@mail.tku.edu.tw

MICHELE MARIS

INAF - Osservatorio Astronomico di Trieste, Via G.B. Tiepolo 11, Trieste, Italy
maris@oats.inaf.it

SILVIA MASI

Dipartimento di Fisica, Università La Sapienza, P. le A. Moro 2, I–00185 Roma, Italy
silvia.masi@roma1.infn.it

ANIELLO MENNELLA

Dipartimento di Fisica, Università degli Studi di Milano, Via Celoria, 16, Milano, Italy
INAF/IASF Milano, Via E. Bassini 15, Milano, Italy
aniello.mennella@fisica.unimi.it

PAOLO NATOLI

Dipartimento di Fisica e Scienze della Terra, Università degli Studi di Ferrara,
Via Giuseppe Saragat 1, I-44122 Ferrara, Italy
INAF–IASF Bologna, Via Piero Gobetti 101, I-40129 Bologna, Italy
paolo.natoli@gmail.com

HANS ULRIK NORGAARD-NIELSEN

DTU Space, Elektrovej, DK - 2800 Kgs. Lyngby, Denmark
hunn@space.dtu.dk

ETIENNE POINTECOUTEAU

CNRS, IRAP, 9 Av. colonel Roche, BP 44346, F-31028 Toulouse cedex 4, France
Université deToulouse, UPS-OMP, IRAP, F-31028 Toulouse cedex 4, France
etienne.pointecouteau@irap.omp.eu

YOEL REPHAELI

School of Physics, Tel Aviv University, Tel Aviv 69978, Israel
CASS, University of California, San Diego, La Jolla, CA 92093, USA
yoelr@wise.tau.ac.il

LUIGI TOFFOLATTI

Departamento de Física, Universidad de Oviedo, c. Calvo Sotelo s/n, 33007 Oviedo, Spain
IFCA-CSIC, Instituto de Física de Cantabria, avda. Los Castros s/n, 39005 Santander, Spain
ltoffolatti@uniovi.es

In this article we focus on the astrophysical results and the related cosmological implications derived from recent microwave surveys, with emphasis to those coming from the *Planck* mission. We critically discuss the impact of systematics effects and the role of methods to separate the cosmic microwave background signal from the astrophysical emissions and each different astrophysical component from the others. We then review of the state of the art in diffuse emissions, extragalactic sources, cosmic infrared background, and galaxy clusters, addressing the information they provide to our global view of the cosmic structure evolution and for some crucial physical parameters, as the neutrino mass. Finally, we present three different kinds of scientific perspectives for fundamental

physics and cosmology offered by the analysis of on-going and future cosmic microwave background projects at different angular scales dedicated to anisotropies in total intensity and polarization and to absolute temperature.

Keywords: cosmology, cosmic background radiation, galaxy clusters, active galaxies, primordial galaxies, Milky Way, Zodiacal Light.

1. Introduction

Since its discovery, the cosmic microwave background (CMB) represents a crucial probe for our general view of the Universe and the understanding of key aspects in cosmology and fundamental physics. Furthermore, microwave surveys are becoming more and more relevant for the comprehension of the physical and evolutionary properties of astrophysical structures at different cosmic epochs, from galactic to cosmological scales. Following the very important results from balloon-borne experiments, the NASA COBE and WMAP satellites, and recent ground-based projects, covering together a wide multipole range, the available and forthcoming data products from the *Planck* mission[a] will have a strong impact in these fields in the coming decades[b]. *Planck* instruments are in fact the most sensitive microwave receivers ever launched in space. Their sensitivity calls for a comparable level of systematic effect control, one of the main drivers in satellite and instrument design and currently key in data reduction and interpretation[1–4], a topic addressed in Section 2. Similarly, for high sensitive microwave observations, the accuracy in the recovery of the CMB properties largely relies on the capability to disentangle the cosmological signal from the astrophysical emissions (the so-called foregrounds), as discussed in Section 3. Waiting for the *Planck* cosmological results, we focus here on currently available astrophysical discoveries based on the first *Planck* surveys possibly complemented by other sets of observations carried out at similar wavelengths and combined with surveys in other frequency domains, in a multifrequency approach. Section 4 is devoted to the diffuse emissions coming from the Solar System and the Galaxy, on the physical processes operating at various Galactic scales, and on their manifestation at microwave wavelengths. In Section 5 we discuss the main properties derived on extragalactic sources at different cosmic distances, including the main evidencies regarding the cosmic infrared background. Section 6 is dedicated to the recent observational results on galaxy clusters and on their scaling relations, with the wealth of information they provide on baryon physics and their use as a probe for neutrino mass estimation. Finally, in Section 7 we review three different topics in CMB

[a] *Planck* is a project of the European Space Agency - ESA - with instruments provided by two scientific Consortia funded by ESA member states (in particular the lead countries: France and Italy) with contributions from NASA (USA), and telescope reflectors provided in a collaboration between ESA and a scientific Consortium led and funded by Denmark.

[b] This paper is based largely on the *Planck* Early Release Compact Source Catalogue and publicly available publications by ESA and the *Planck* Collaboration, for what concerns the related aspects. Any material presented here that is not already described in *Planck* Collaboration papers represents the views of the authors and not necessarily those of the *Planck* Collaboration.

cosmology, possibly linked to fundamental physics, that will be addressed respectively by the forthcoming results from the *Planck* mission, by future high resolution ground-based experiments, and by the next generation of CMB spectrum projects.

2. Control, assessment and removal of systematic effects in *Planck*

Planck orbits around the L2 Lagrangian point and scans the sky spinning at 1 rpm in almost great circles with its Gregorian dual-reflector telescope pointing at 85° from the spin axis[5,6] . In the telescope focal plane the microwave photons are collected by two wide-band receiver arrays spanning a frequency interval ranging from ∼30 GHz to ∼857 GHz. The Low Frequency Instrument (LFI), is a coherent differential array based on 20 K InP HEMT[c] amplifiers currently working in three bands centered at approximately 30, 44 and 70 GHz [7] . The High Frequency Instrument is an array of bolometers cooled to 0.1 K operating at six frequency bands centered at 100, 143, 217, 353, 545 and 857 GHz [8] . *Planck* (full width half maximum, FWHM) resolution ranges from $33.3'$ to $4.3'$ going from 30 GHz to 857 GHz, and its final sensitivity per (FWHM^2 resolution element is in the range of $\sim 2-14$ μK/K in terms of $\delta T/T$ for frequencies $\nu \leq 353$GHz. The life of *Planck* largely exceeded the early plan. Five all-sky surveys has been accumulated with HFI, while LFI is planned to operate up to about the end of Summer 2013, so completing eight all-sky surveys.

In Table 1 we list the main systematic effects in *Planck* according to their source and provide few notes about their control and residual impact on science.

In the LFI we have generated timelines, maps and power spectra of thermal effects and 1-Hz spikes using in-flight scientific and housekeeping data coupled with transfer functions measured during ground tests. Table 2 reports the peak-to-peak and rms effect on full-sky temperature maps of these effects, while in Fig. 1 we show their expected temperature angular power spectra after component separation. The effect of component separation (see next section) has been reproduced by mixing the systematic effects maps using the same mixing matrix used to extract the *Planck* CMB map (not reported in this paper) from the individual frequency maps.

Our current analysis confirms that the level of systematic effects rejection is in line with pre-launch expectations and will allow full exploitation of the science encoded in the CMB signal.

3. Component separation

As widely discussed in the next section, the sky emission, at a given frequency, is a superposition of emission from various sources. The plausible contamination of the observable primary CMB by foreground emission has always been a source of concern for CMB observations. However, the level of foreground contamination, at high Galactic latitude and at frequencies between 50 and 200 GHz, is low enough that for ℓ less than about 2500 the temperature (or total intensity) APS, C_ℓ^{TT},

[c]Indium Phosphide High Electron Mobility Transistor

Table 1. Main systematic effects in *Planck*

Category	Effect	Notes
Optics[9,10]		
	Side-lobes	Galaxy and CMB dipole pickup by main and sub-reflector spillovers. Negligible effect on temperature maps, needs to be removed at low frequency for polarization analysis.
Detectors		
	Cosmic ray hits	Affect bolometric detectors. Removed from timelines via template fitting.
	$1/f$ noise	Affects radiometric and bolometric detectors. In the LFI the $1/f$ contribution is limited to max 3% by differential measurement strategy and de-striping algorithms[11] .
	Bandpass mismatch[12]	Affects primarily radiometric detectors. Negligible impact on temperature. Corrected in polarisation at map level exploiting polarized source measurements (Crab Nebula).
Electronics		
	1-Hz spikes	Affects LFI data. Removed from timelines by template fitting.
Thermal†		
	300 K fluctuations	In principle affect both instruments. Inherent hardware stability is compliant with scientific requirements.
	20 K fluctuations	Affect mainly LFI. Inherent hardware stability is compliant with scientific requirements.
	4 K fluctuations	Affect both instruments. Inherent hardware stability is compliant with scientific requirements.

†In the LFI a combination of the differential measurement strategy with calibration and de-striping further reduce the effect.

Table 2. Effect on *Planck* LFI maps of the main systematic effects

	30 GHz [μK]		44 GHz [μK]		70 GHz [μK]	
Channel	p-p	rms	p-p	rms	p-p	rms
1-Hz spikes . .	4.00	0.45	1.51	0.15	2.56	0.30
Thermal fluct						
Back-end	1.27	0.11	0.63	0.05	2.70	0.24
Front-end	1.05	0.23	1.15	0.22	1.12	0.21
4 K loads	9.76	0.98	9.73	0.98	1.30	0.16
Total	10.92	1.10	9.73	0.98	4.28	0.45

can be accurately measured with only minor masking of the regions most contaminated by foregrounds (Galactic interstellar medium (ISM) and bright extragalactic compact sources). On smaller scales, emission from a background of blended faint extragalactic sources contributes a significant fraction of the observed power[13–15] .

For a sensitive mission such as *Planck*, foreground emission, rather than instrumental noise, sets the limit of the accuracy of the measurement of the CMB APS. This limit depends on the effectiveness of any foreground-cleaning technique

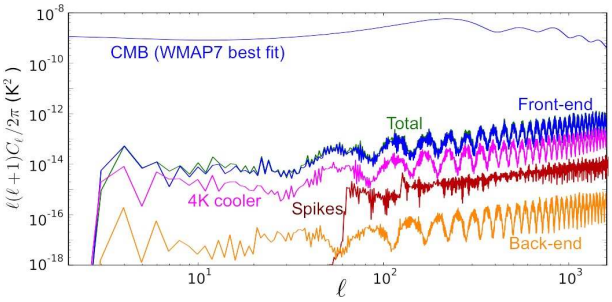

Fig. 1. Impact of main systematic effects in *Planck* LFI on temperature angular power spectrum (APS) as function of the multipole ℓ.

used to separate the primary CMB emission from foregrounds. Hence, the development, comparison, and optimization of component separation methods has been an important activity in the *Planck* Collaboration during the preparation of the mission[16–19] .

3.1. *Modeling sky emission*

A multicomponent model of sky emission serves both as a framework for analyzing and interpreting the observations, and as a summary of our knowledge about the astrophysical emitters. Recently, such a model of sky emission, the *Planck* Sky Model (PSM), has been put together for this purpose[20] . It is based on an underlying ΛCDM cosmological model with associated standard parameters[d]. In this framework, the emission of the CMB, of galaxy clusters, and of high-redshift galaxies in haloes of large-scale density contrast, is described on the basis of their statistical properties (angular power spectra of the CMB, cluster number counts, source number counts and halo occupation distribution as a function of luminosity, of redshift, and of spectral energy distribution). Known bright radio and infrared sources are modeled using extrapolations of their measured fluxes at various frequencies. Galactic diffuse emission is modeled as a mixture of several components: synchrotron radiation from energetic electrons spiraling in the Galactic magnetic field, thermal dust emission, free-free (Bremsstrahlung) emission from the warm interstellar medium, the so-called 'anomalous' dust emission from small spinning dust grains. Molecular line emission could also contribute to the signal in some frequency bands, that are typically relatively wide in order to increase the measurement sensitivities. In particular, the emission from the CO line is clearly seen in *Planck* data sets that allow to produce all-sky accurate maps of this signal[4] .

[d]The spectral index and amplitude of scalar perturbation, n_s and A_s, the ratio between the amplitude of tensor and scalar perturbations, $r = A_t/A_s$, the density parameters of matter, baryons, dark energy, Ω_m, Ω_b, Ω_Λ, the Hubble constant, H_0, etc., the default values of which are set to the current best fit.

3.2. *Basics of component separation*

Consider a single pixel p in a set of maps observed at various frequencies, indexed by ν. The signal observed at frequency ν, in pixel p, can be written as

$$x(\nu, p) = \sum_i a_i(\nu, p)\, s_i(p) + n(\nu, p), \tag{1}$$

or, in vector-matrix format

$$\mathbf{x}(p) = \mathsf{A}(p)\, \mathbf{s}(p) + \mathbf{n}(p). \tag{2}$$

If we know the frequency dependence $\mathsf{A}(p)$ of each foreground in pixel p, our problem is just to invert a (set of) linear system(s) to find the reference component templates $\mathbf{s}(p)$. In the limit where the instrumental noise $\mathbf{n}(p)$ is small, the inversion is implemented using the inverse of A (or, for non-square systems, the left pseudo-inverse $\mathsf{A}^{-1}_{\rm left} = [\mathsf{A}^t\mathsf{A}]^{-1}\mathsf{A}^t$). Otherwise, classical linear solutions such as least square (LS) or Wiener inversion can be used. They require, however, the prior knowledge of the covariance matrix $\mathsf{R}_n(p)$ of the instrumental noise in each pixel, and possibly also of that of the signal, $\mathsf{R}_s(p)$. The LS solution is

$$\widehat{\mathbf{s}}_{\rm LS}(p) = \left[\mathsf{A}^t\mathsf{R}_n^{-1}\mathsf{A}\right]^{-1} \mathsf{A}^t\mathsf{R}_n^{-1}\mathbf{x}(p), \tag{3}$$

and the Wiener one is

$$\widehat{\mathbf{s}}_{\rm Wiener}(p) = \left[\mathsf{A}^t\mathsf{R}_n^{-1}\mathsf{A} + \mathsf{R}_s^{-1}\right]^{-1} \mathsf{A}^t\mathsf{R}_n^{-1}\mathbf{x}(p), \tag{4}$$

where A^t denotes the transpose of A. Most of the time however, neither the 'mixing matrix' A, nor the statistical properties of the signal, are known. Sometimes even the noise covariance is not well known. One must then find a way to estimate them from the data themselves prior to inverting the linear mixture and recovering an estimate of each of the components.

3.3. *Blind component separation*

Blind separation of linear mixtures is a classical field of research in signal and image processing. Typically, the data model is of the form of Eq. (2), except that A does not depend on p, and noise is often not an issue. The main problem is then to decide how many components exist in the data, and determine A (or find a matrix W that inverts the system, without explicitly estimating A). The main idea is to use the (assumed) statistical independence of the various components $\mathbf{s}$. Blind component separation applied to CMB observations must address specific issues: error estimation, ill-conditioned covariance matrices, correlations between some of the components, spherical data sets. This has led the CMB community to adapt classical independent component analysis (ICA) methods for their analyses.

The FastICA method[21,22] aims at inverting the linear system using the matrix W that maximizes a measure of the non-Gaussianity of the component maps. The

method, however, is not very effective at distinguishing Gaussian CMB from Gaussian noise. It also fails to exploit the strong spatial correlation of the CMB and of most of the diffuse foreground emission.

Spectral matching ICA (SMICA)[23–25], is a flexible method that maximizes the likelihood of a parametric model of A, R_s and R_s by minimizing the spectral mismatch between empirical and modeled second-order statistics of the observed maps. It is particularly useful for measuring a CMB APS, or parameters that model it, directly from multifrequency data. It has been used for predicting the errors on the tensor to scalar ratio r that can be reached by future CMB B-modes experiments[26]. Very similar in spirit, although many implementation details vary, the correlated component analysis (CCA) method has been developed to deal specifically with correlated components[27]. Once second-order statistics of components and noise are obtained, they are used to invert the linear system.

Neural networks provide another attractive solution for finding either coefficients that invert the linear mixture, or only those coefficients that recover the CMB specifically[28]. The method seems to perform well both on simulations[29] and on real data[30]. The impact of the training of the neural network, however, is hard to evaluate, and the propagation of errors not straightforward. These two limitations are serious for CMB data analysis, and may explain why the method has not received more attention so far.

A completely different point of view is taken in [31]. Instead of learning (explicitly or implicitly) the model (or part of it) in the data themselves, a parametric model of all relevant foregrounds is assumed a priori. Specifically, an amplitude and parameters defining an appropriate emission law are assigned to each emission process in each sky pixel. The value of all parameters are then found using a Monte-Carlo Markov chain (MCMC) algorithm. This is clearly the appropriate approach for measuring efficiently parameters of a known model, and is hence of much interest for component separation. It is also very flexible, as the foreground model can be chosen freely. The main caveat is that while in theory this method provides a complete likelihood (and hence errors) for all parameters, in practice the main uncertainty is whether the assumed parametric model is correct. Goodness of fit is not a fully satisfactory criterion: as well known, it is always possible to fit a limited data set with a wrong model, provided the number of parameters used in the fit is large enough. The method is hence of interest only when many different channels of observation are available. An alternative implementation of this idea has been proposed by [32].

Finally, yet another approach, based on a different optimization criterion to recover the mixing matrix A, has been proposed by [33]. It uses a likelihood penalization imposing a sparse representation of sky components in some over-complete dictionary of functions that serve as a redundant basis. The first implementation of the method, although promising and conceptually interesting, was not optimized for real-life data processing, due to lack of proper handling of different map resolutions and of the non-stationarity of the component emissions. This has been improved

with a recent version that uses wavelet decompositions, allowing variations in both pixel and harmonic space of the linear combinations of the maps used for CMB recovery[34]. Such localization makes it possible to relax the restrictive condition that the emission of each component should be decomposable into the product of a pixel-independent emission law $A(\nu)$ and a spatial template $s(p)$.

3.4. *The internal linear combination and variants*

Bypassing in some way the need to rely on a specific model of all foreground emission (especially rigid linear mixtures in which A does not depend on p) is an appealing option. The frequency scaling of CMB anisotropies themselves being known to be the derivative with respect to temperature of a 2.725 K blackbody, independently of p, one may write a simplified model of the observed maps as

$$\mathbf{x}(p) = \mathbf{a}\, s(p) + \mathbf{n}(p), \tag{5}$$

where $s(p)$ is the CMB map, $\mathbf{a}$ the CMB frequency scaling, and all the unknown (or poorly known) noise and foreground contamination is dumped together into a single noise term $\mathbf{n}(p)$. The LS reconstruction of the CMB map is then

$$\widehat{\mathbf{s}}_{\rm LS}(p) = \frac{\mathbf{a}^t \mathsf{R}_n^{-1} \mathbf{x}(p)}{\mathbf{a}^t \mathsf{R}_n^{-1} \mathbf{a}}. \tag{6}$$

This may seem impossible to implement without knowing R_n (which now includes unknown foregrounds correlated between channels). However, under the hypothesis that $s(p)$ is not correlated with $\mathbf{n}(p)$, the covariance R_x of the observed maps is $\mathsf{R}_x = \sigma_s^2 \mathbf{a}\mathbf{a}^t + \mathsf{R}_n$, where σ_s^2 is the variance of the CMB map. It is then straightforward to show, using the Woodburry inversion formula, that $\mathbf{a}^t \mathsf{R}_x^{-1} \propto \mathbf{a}^t \mathsf{R}_n^{-1}$, and hence that the LS solution can be rewritten as

$$\widehat{\mathbf{s}}_{\rm LS}(p) = \frac{\mathbf{a}^t \mathsf{R}_x^{-1} \mathbf{x}(p)}{\mathbf{a}^t \mathsf{R}_x^{-1} \mathbf{a}}. \tag{7}$$

This form is easily implemented using empirical estimates $\widehat{\mathsf{R}}_x$ of R_x obtained on the data themselves. This solution is also obtained as the constrained minimization problem of finding the linear combination $\mathbf{w}^t \mathbf{x}$ of the inputs that has minimum variance under the 'CMB preserving' condition $\mathbf{w}^t \mathbf{a} = 1$. It is classically called the internal linear combination (ILC) method.

The ILC method, for its simplicity and robustness, has been used for the analysis of COBE-DMR, WMAP, and *Planck* data[4,35,36]. Variants that compute weights in different regions of pixel, harmonic or wavelet space for CMB temperature or polarization have been derived[37–40]. Extensions for recovering more components than just the CMB are discussed by [41,42].

It is important to note that the ILC is prone to subtle biases, which must be understood and controlled for scientific analyses based on ILC maps. The first bias, a loss of some modes of the original CMB and hence of CMB power, is due to empirical correlations between the CMB and the contaminants, and is discussed at

length in the appendix of [38]. The second is an amplification of calibration errors in the observed channels (or errors in the assumed frequency scaling of the component of interest), and is discussed in detail by [43].

3.5. *Error assessment and masking*

One of the most crucial questions, once the component separation is performed, is the assessment of errors. How well does a method perform? While it is easy to propagate errors in a fit, the problem in component separation is that modeling errors dominate the uncertainties. Nonetheless, three approaches can give an idea of component separation performance.

First, one can compare the results obtained with methods that are conceptually very different. If, however, results are very method-dependent, as usual, then one must either explain the differences and discard the method(s) thought to be less effective, or, for the post-analysis of the output map(s), mask (or flag as plausibly contaminated) any sky region in which agreement cannot be achieved.

Second, one may test methods on simulations that are as realistic as possible. This has been one of the original motivations for the development of the PSM. However, the performance of some component separation methods is very sensitive on very subtle details about the sky emission. The refinement of the model and the separation of components are thus two complementary parts of a global, iterative, data analysis chain.

Finally there is a third method, that permits to identify regions of the sky where the number of channels available is not sufficient to separate all emissions. Consider noisy observations of unspecified sky signals, $\mathbf{x}(p) = \mathbf{s}(p) + \mathbf{n}(p)$. Usually, the sky and noise components are pairwise de-correlated, and thus $\mathsf{R}_x = \mathsf{R}_s + \mathsf{R}_n$. We now suppose that R_n (instrumental noise only) is reasonably well known. Then we can whiten the observations (by multiplication by the square root of R_n). For the new data set, we have $\mathsf{R}_x = \mathsf{R}_s + \mathsf{Id}$. In the basis of diagonalisation of R_x, the covariance becomes $\mathsf{R}_x = \Delta + \mathsf{Id}$. The number of (local) eigenvalues of R_x significantly larger than unity is the dimension of the space spanned by measurable signal components. If all eigenvalues are larger than unity, then there are locally more independent astrophysical emissions than can be separated without external information. If, however, only some of the eigenvalues are significantly larger than unity, then in principle the data set is redundant enough for blind component separation, for instance with methods such as SMICA and the ILC which, implemented in wavelet space, are expected to perform very satisfactorily.

4. Diffuse foregrounds

Except for the averaged (monopole) signal, microwave and sub-mm surveys are dominated at large angular scales by the diffuse signals from the Solar System and the Milky Way, emerging as foreground sources with patterns particularly prominent close to the ecliptic and Galactic plane, respectively, and, typically, remarkable up

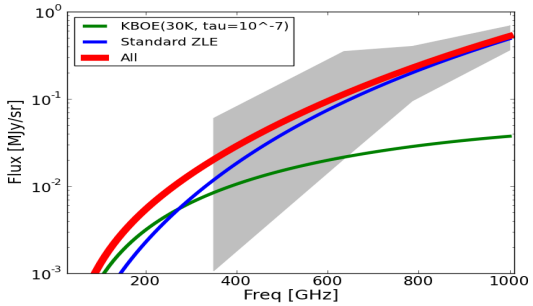

Fig. 2. The expected spectral energy distribution (SED) for the sky averaged ZLE (blue line) and an hypothetical cold dust component with $T_{\rm dust} = 30$ K, $\tau = 10^{-7}$ (green line) and their sum (red line) compared with the COBE/FIRAS spectrum (gray patch).

to few tens of degrees from them. The observer position plays a significant role in the study of the former (while it can be fully neglected for the latter, at least at the angular resolutions relevant here). For this reason, a special care in the application of the component separation methods described in previous section, if not a fully different approach, is required in this case, since, in general, the time dependence of the signal should be accounted for.

4.1. *Solar System diffuse emissions*

Solar System provides the most fore of all the foregrounds. In particular Zodiacal Light Emission (ZLE), i.e. the emission from Interplanetary Dust Particles (IDPs), dominated the sky signal at short wavelengths. At wavelengths shorter than 12 μm ZLE is mainly due to scattering of solar radiation, while at longer wavelengths thermal emission is the most important generation mechanism[44,45] . ZLE is usually not accounted in CMB studies. In fact, since the ZLE flux below 1 THz decreases with ν^4 (see Fig. 2, where the COBE/FIRAS spectrum is provided by [45]), i.e. as a modified blackbody with $T_{\rm dust} = 240$ K, its contribution would be significantly smaller than the others foreground signals at CMB related frequencies.

However Fig. 2 is based just on the observed emission of the IDPs at frequencies above 1 THz, which is dominated by the population of grains between Earth and Jupiter orbits. Given dust orbiting the Sun is removed in short times by Pointing-Robertson decay, radiation pressure, grains–grains collisions and planetary encounters a mechanism to continuously refurbish the population of IDPs is needed. In the inner Solar System the main contributors are comets and asteroids, even if some dust is supposed to come from interstellar space. Other sources of dust are know to be effective far from the Jupiter orbit, in particular the erosion and mutual collisions of trans-Neptunian objects (TNOs) and Kuiper Belt objects (KBOs) produced a second band of dust in the outer Solar System, detected by deep space probes. We will denote with KBOE (Kuiper Belt objects emission) the diffuse emission from this class of IDPs.

Being at heliocentric distances much larger than IDPs responsible for standard ZLE, particles responsible for KBOE would be quite cold having $T_{\rm dust} \approx 30 - 60$ K or lower. The optical depth below 1 THz is unknown. It depends on the balance between the mechanisms of dust production either mutual collisions between larger bodies or erosion by interstellar dust, the former tends to produce larger grains then the latter, the dust collision rate, the composition of dust, the geometrical distribution of dust and the relative efficiency of production and destruction mechanisms. However it hardly will exceeds the optical depth for standard ZLE which is about 10^{-7}. Two reasons make hard the detection of KBOE: (*i*) at high frequencies the ZLE emission would overwhelm the KBOE, as evident from the example of SED in Fig. 2; (*ii*) the main method to separate the ZLE from background emission, basically from Galactic dust, is to measure the seasonal dependence of ZLE signal for a fixed line–of–view, as the observer moves within the Solar System while surveying the sky. Such effect amounts to at most 7% of the emission, more than 90% of the modulation comes from dust within 3 AU from the Earth, so that the seasonal dependence from dust at heliocentric radii of 50 AU would be largely negligible.

It is evident how Solar System diffuse emission may act as a foreground for CMB in two ways. The simplest case is when templates for Galactic and extragalactic emission at frequencies relevant for CMB observations are extrapolated from maps obtained at wavelengths where the ZLE is an important source of systematics. This is typical of CMB observations at frequencies higher than 100 GHz, where a template dust map is needed. Such maps are produced by extrapolating at CMB frequencies maps from observations made at several tens of μm where the ZLE is very strong and must be removed. In this case the ZLE will represent a sort of indirect foreground whose exact impact on CMB will depend. The other possibility is that of a direct impact on CMB missions of an un-removed component which is relevant at CMB frequencies, such as the KBOE. In this case the exact effect will depend on the level of contamination compared to the level of the CMB fluctuations, on the spatial pattern, and on its combination with the CMB.

A simple argument allows us to estimate the effect of un-removed ZLE or KBOE on the CMB APS at different multipoles. Let us to consider a sky with just ZLE or KBOE and an observatory scanning the sky to form maps. Due to unavoidable geometrical constrains, the observed sky regions are more or less tightly correlated to specific positions in the Solar System, but it is not possible to grant a one–to–one correlation, so that when timelines are co-added to form maps the result will be a distribution with small discontinuities, and in general different scanning strategies will create slightly different maps[46] . However, if observations from many scans, spanning several years, are co-added, then a smooth map with a very strong planar symmetry about the ecliptic will be obtained. Denoting with $a_{\ell,m,\rm SS}$ the coefficients of the spherical harmonics (SH) expansion for such map, the planar symmetry assures that in a reference frame defined by this plane $a_{\ell,m,\rm SS} \equiv 0$ for any odd ℓ or for any $m \neq 0$, so that $C_\ell^{\rm SS} = {a_{\ell,0}^{\rm SS}}^2/(2\ell+1)$ for even ℓ and zeros for odd ℓ. The combined map with CMB will be unchanged for odd ℓ while will have in the

same reference frame $C_\ell = C_\ell^{\rm CMB} + C_\ell^{\rm SS} + a_{\ell,0}^{\rm SS} a_{\ell,0}^{\rm CMB}/(2\ell+1)$. So, depending on the signs of the ZLE or KBOE and CMB components, C_ℓ can be smaller or larger than $C_\ell^{\rm CMB}$. Therefore, it can not be in principle excluded that part of the anomalies seen at low multipoles can be ascribed to some unknown and un-removed component of the ZLE or KBOE[47] and/or to interplay between this foreground and un-removed dipole-like systematic effects[48] , especially at low ℓ where a Solar System large scale diffuse emission should have the maximum power.

4.2. *Galactic emissions*

The wide frequency coverage of *Planck* when taken with relevant ancillary data provides a unique opportunity to characterize all the relevant Galactic foreground components. Of particular interest is the recently identified anomalous microwave emission (AME) due to spinning dust which has an important contribution at the lower *Planck* frequencies. Inclusion of this component has a domino effect on the spectrum of the other components, particularly at frequency $\nu \lesssim 100$GHz, where synchrotron and free-free emissions are particularly important. The emission from thermal (vibrational) dust dominates at $\nu \gtrsim 70$GHz, but, although weak, it must be considered also at lower frequencies. It should be remembered that the minimum of the Galactic foreground to the CMB is in the range 60–100 GHz where each of these four components can have a small but significant contribution.

4.2.1. *Synchrotron emission*

Synchrotron emission originates in relativistic cosmic ray electrons spiraling in the Galactic magnetic field. The relativistic electrons are produced in the shocks associated with supernova explosions. The spectrum of the synchrotron radio emission is related to the energy spectrum of the relativistic electrons. Up to several GHz the brightness temperature spectral index is ~ -2.7 [49] ; above this frequency it steepens to -3.0 or more at the lower *Planck* frequencies[50] . Another characteristic of synchrotron emission is its linear polarization which is orthogonal to the magnetic field direction; this may be as high as 70 % for an aligned field with a brightness spectrum of -3.0. In the more tangled field environment on the Galactic plane the observed values are in the range 10–50 %.

The current study of the emission of the plane in the inner Galaxy identified the synchrotron component by using component separation techniques. The low frequency data (0.4 to 2.3 GHz) revealed a narrow component in Galactic latitude with a FWHM of 1.6°. This newly identified component is also clearly identified in K and Ka band polarization data from *WMAP*; it has a brightness spectral index of -3.2 [50] . This narrow distribution is the sum of the supernova remnants (SNRs) over the last 10^5–10^6 years (the timescale of the SNRs before they expand into the broader latitude distribution. A similar latitude width is found for the normal ($\sim$1 second period) pulsars; their ages are also $\sim 10^5$–10^6 years. Over this timescale both

the SNR shells and the pulsar proper motions will have taken them to a FWHP of 1.6°, double the width of the nascent OB star distribution (0.9°).

4.2.2. *Free-free emission*

The free-free emission in the inner Galaxy arises from the ionized (electron) gas component produced principally by the hot O and B stars which are confined to a narrow latitude width of 0.9°FWHM. Cooler stars also contribute to the interstellar radiation field (ISRF) which is more diffuse. At intermediate and high latitudes the free-free emission is measured by the Hα spectral line. Even here a correction is needed to account for the absorption of Hα by dust. On the Galactic plane the dust obscuration is so great that the Hα emission line cannot be used. Here the radio recombination lines (RRLs) save the day. No dust absorption correction is required. However an electron temperature is needed to determine the emission measure (EM $= n_e^2 L$) in order to derive the corresponding continuum temperature at any frequency[51] . The brightness temperature spectral index is well determined at *Planck* frequencies; it is ~ -2.13 at 30 GHz. The electron temperature of the diffuse ionized gas appears to be similar to the average for the compact HII regions[52,53] .

The FWHM of the free-free (1.1°) is intermediate between that of OB stars (0.9°) and the neutral hydrogen (1.8°). This is not unexpected since the gas (HI, H2 and dust) density is greatest on the plane and also because the ionized emission is proportional to $n_e^2 L$. The free-free, along with the AME, dominates the emission on the plane in the inner Galaxy.

4.2.3. *Anomalous Microwave Emission (AME)*

AME is the recently identified emission component which is well-correlated with far-infrared (FIR) dust emission. It is produced by rapidly spinning small dust grains having an electric dipole moment[54] . Typical masses are ∼50 atoms which in a dust cloud produce a spectrum which peaks in the range 15–50 GHz depending on the environment and radiation field. *Planck* has for the first time been able to define the shape of the spectrum on the high frequency side of the emission peak in a number of dust/molecular/HII regions, as shown in [55]. This work has provided a rich source of data to explore the emission mechanism in detail.

On the Galactic plane the AME spectrum can be estimated by applying component separation techniques to the strong signals measured here. The AME is the residual emission after the free-free, the synchrotron and the thermal dust have been accounted for. In the frequency range 20–40 GHz AME is comparable in brightness to the free-free for the inner Galactic plane from l = 300°–0°–60°. The latitude width of the emission at these frequencies is similar to that of the thermal dust.

4.2.4. *Thermal dust emission*

The FIR dust spectrum is due to the vibrational emission from dust grains heated by the ISRF. The peak in the emission is at a wavelength of ∼60–100 microns. Averaged over the intermediate latitude sky the dust temperature is ∼18 K with a grey body slope in brightness of +1.7 [56] . On the Galactic plane the dust temperature is somewhat higher at 20–24 K. The latitude width of the dust emission at say 100 microns is 1.2°, similar to that of CO (representing H_2). The narrower width compared with HI is probably due to the higher dust temperature on the plane produced by the O and B stars.

4.2.5. *Emissions close to the Galactic plane*

We find a narrow latitude distribution on the Galactic plane for each of the four emission components, synchrotron, free-free, AME and thermal dust. Recent star formation over the last 10^5–10^6 years in the dense gas regions on the plane is most likely the cause.

Using precise full-sky observations from *Planck*, and applying several methods of component separation, the emission from the Galactic "haze" at microwave wavelengths has been identified and characterized[57] . The haze is a distinct component of diffuse Galactic emission, roughly centered on the Galactic centre, and extends to $|b| \sim 35°$ in Galactic latitude and $|l| \sim 15°$ in longitude. By combining WMAP and *Planck* data, [57] were able to determine the spectrum of this emission to high accuracy, unhindered by the large systematic biases present in previous analyses. The derived spectrum is consistent with power-law emission with a spectral index of -2.55 ± 0.05, thus excluding free-free emission as the source and instead favoring hard-spectrum synchrotron radiation from an electron population with a spectrum (number density per energy) $dN/dE \sim E^{-2.1}$. At Galactic latitudes $|b| < 30°$, the microwave haze morphology is consistent with that of the Fermi gamma-ray "haze" or "bubbles" (see also [58]), indicating that we have a multi-wavelength view of a distinct component of our Galaxy. Given both the very hard spectrum and the extended nature of the emission, it is highly unlikely that the haze electrons result from supernova shocks in the Galactic disk. Instead, a new mechanism for cosmic-ray acceleration in the centre of our Galaxy is implied.

The wide frequency coverage of *Planck*, which includes polarization, allows the spectrum of each component to be determined unambiguously. Polarization data from *Planck* are awaited with considerable interest.

5. Extragalactic radio and far–IR sources at mm/sub-mm wavelengths

The *Planck* Early Release Compact Source Catalogue (ERCSC)[59] – the *first complete full-sky catalogue* of bright sub-millimeter extragalactic compact sources – provides positions and flux densities of hundreds of "radio" sources (intermediate to

high–redshift Active Galactic Nuclei (AGN)) and of thousands of "far-IR" sources (low–redshift dusty galaxies) detected in each of the nine *Planck* frequency maps during the first 1.6 *Planck* full-sky surveys. As shown in [59], their Table 1, the full-sky surveys of the *Planck* satellite are – and will be, for years to come – unique in the millimeter, at $\lambda \leq 3$ mm, and sub-millimeter domains. Thanks to this huge amount of new data it is thus possible to investigate the SEDs of extragalactic point sources in a spectral domain very poorly explored before and, at the same time, their cosmological evolution, at least for some relevant source populations.

5.1. *Radio sources: "blazars"*

The most recent estimates on source number counts of extragalactic radio (synchrotron) sources up to $\sim 50 - 70$ GHz, and the optical identifications of the corresponding point sources (see e.g. [60]), show that these counts are dominated by radio sources whose average spectral index is "flat", i.e., $\alpha \simeq 0.0$ (with the usual convention $S_\nu \propto \nu^\alpha$). This result confirms that the underlying source population is essentially made of Flat Spectrum Radio Quasars (FSRQ) and BL Lac objects, collectively called "blazars"[e], with minor contributions coming from other source populations[62,63] . At frequencies > 100 GHz, however, there is now new information for sources with flux densities below about 1 Jy, coming from the South Pole Telescope (SPT) collaboration[64] , with surveys over 87 deg^2 at 150 and 220 GHz, and from the Atacama Cosmology Telescope (ACT) survey over 455 deg^2 at 148 GHz [65] .

To study the spectral properties of the extragalactic radio sources in the *Planck* ERCSC[66] used a reference 30 GHz sample above an estimated completeness limit $S_{lim} \simeq 1.0$ Jy. In this sample, the 30–143 GHz median spectral index is in very good agreement with the one found by Marriage et al.[65] for their bright ($S_\nu > 50$ mJy) 148 GHz-selected sample with complete cross-identifications from the Australia Telescope 20 GHz survey, i.e $\alpha_{20}^{148} = -0.39 \pm 0.04$. In the whole, the results of [66] show that in their sample selected at 30 GHz a moderate steepening of the spectral indices of the radio sources at high radio frequencies, i.e. $\geq 70 - 100$ GHz, is clearly apparent. It has also been shown by [66] that differential number counts at 30, 44, and 70 GHz are in good agreement with those derived from *WMAP* data[67] at nearby frequencies. The model proposed by de Zotti et al.[63] in 2005 is consistent with the present counts at frequencies up to 70 GHz, but over-predicts the counts at higher frequencies by a factor of about 2.0 at 143 GHz and about 2.6 at 217 GHz. As reminded before, the analysis of the spectral index distribution over different frequency intervals, within the uniquely broad range covered by *Planck* in the mm and sub-mm domain, has highlighted an average *steepening* of source spectra above about 70 GHz. This steepening accounts for the discrepancy between the model predictions of de Zotti et al.[63] and the observed differential number counts at HFI

[e]Blazars are jet-dominated extragalactic objects characterized by a strongly variable and polarized emission of the non-thermal radiation, from low radio energies up to high energy gamma rays; see e.g. [61].

frequencies.

Recently, a successful explanation of the change detected in the spectral behavior of extragalactic radio sources (ERS) at frequencies above 70-80 GHz has been proposed by Tucci et al.[68] . By applying the Königl[69] model for the emission in the inner jets of blazars, [68] makes a first attempt at constraining the most relevant physical parameters that characterize the emission of blazar sources by using the number counts and the spectral properties of extragalactic radio sources estimated from high–frequency radio surveys[f]. As noted before, a relevant steepening in blazar spectra with emerging spectral indices in the interval between -0.5 and -1.2, is commonly observed at mm/sub-mm wavelengths. Tucci et al.[68] interpreted this spectral behavior as caused, at least partially, by the transition from the optically–thick to the optically–thin regime in the observed synchrotron emission of AGN jets[70] , giving rise to a "break" frequency, ν_M, typically in the range between 50-2000 GHz, at which the synchrotron spectrum of jets bends down[g]. On the whole, the results of [68] imply that the parameter r_M should be of parsec–scales, at least for FSRQs, in agreement with theoretical predictions[71] , whereas values of $r_M \ll 1$ pc should be only typical of BL Lac objects or of rare, and compact, quasar sources.

5.2. *Far–IR sources: local dusty galaxies*

The analysis done by [72] presented the first results on the properties of nearby galaxies using ERCSC data. From reliable associations between *Planck* and IRAS, they selected a subset of 468 for SED studies, namely those with strong detections in the three highest frequency *Planck* bands and no evidence of cirrus contamination. This selection has thus provided a first *Planck* sample of local, i.e. at redshift < 0.1, dusty galaxies [h]. The analysis of SEDs of these local galaxies[72] has confirmed the presence of cold dust in local giant and, largely, in dwarf galaxies[i]. In [72] it is also found that some local galaxies are both luminous and cool, with properties similar to those of the distant SMGs uncovered in deep sub-mm surveys. The main conclusion of [72] is that cold ($T < 20$ K) dust is thus a significant and largely unexplored component of many nearby galaxies and that there is a new population of cool

[f]The main goal of [68] was to present physically grounded models to extrapolate the number counts of ERS, observationally determined over very large flux density intervals at cm wavelengths down to mm wavelengths, where experiments aimed at accurately measuring CMB anisotropies are carried out.

[g]Based on published models, Tucci et al.[68] estimated the value of the frequency ν_M (and of the corresponding radius r_M) at which the break occurs on the basis of the ERS flux densities measured at 5 GHz and of the most typical values for the relevant physical parameters of AGN jets.

[h]This sample is very important for determining their emission properties and, in particular, the presence of different dust components contributing to their sub-mm SEDs.

[i]The SEDs are fitted using parametric dust models to determine the range of dust temperatures and emissivities. They found evidence for colder dust than has previously been found in external galaxies, with temperatures $T < 20$ K. Such cold temperatures are found by using both the standard single temperature dust model with variable emissivity β, or a two dust temperature model with β fixed at 2.

sub-mm galaxies, showing the presence of even cooler dust grains, with estimated temperatures of ∼10-13 K.

Very recently, using selected samples from the first *Planck* 1.6 full-sky surveys, i.e. the *Planck* ERCSC, [73] derived number counts of extragalactic point sources from 100 to 857 GHz (3 mm to 350 μm). More specifically, for the first time, number counts have been provided of synchrotron dominated sources (blazars) at high *Planck* frequencies (353 to 857 GHz) and of dusty galaxies at lower frequencies (217 and 353 GHz). *Planck* number counts are found to be in the Euclidean regime in this frequency range, since the ERCSC comprises only bright sources ($S > 0.3$ Jy). The estimated number counts appear generally in agreement with other data sets, when available (see [73] for more details).

These new estimates of number counts of synchrotron and of dust–dominated extragalactic sources allowed new constraints to be placed on cosmological evolution models which extend their predictions to bright flux densities, i.e. $S > 1$ Jy. A very relevant result is that the most successful model of Tucci et al.[68] is performing particularly well at reproducing the number counts of synchrotron–dominated sources up to 545 GHz. On the contrary, [73] highlights the failure of many models for number count predictions of dusty galaxies to reproduce all the high-frequency counts. The likely origin of these discrepancies is an inaccurate description of the galaxy SEDs used at low redshift in these models. Indeed a cold dust component, detected by [72] , is rarely included in the models of galaxy SEDs at low redshift. On the whole, these results already obtained by the exploitation of the *Planck* ERCSC data are providing valuable information about the ubiquity of cold dust in the local Universe, at least in statistical terms, and are guiding to a better understanding of the cosmological evolution of extragalactic point sources at mm/sub-mm wavelengths.

5.3. *Nearby galaxies: the case of M31*

As discussed above, WMAP and *Planck* data can be used to get information about point like astrophysical sources (see e.g. [74] and references therein), including nearby galaxies. Recently, the 7-year WMAP data have been used to trace the disk and the halo of the M31 galaxy[75] . Unexpectedly, an asymmetry in the mean microwave temperature towards both the M31 disk and halo, along the direction of the M31 rotation, has been found. The maximum temperature contrast (see Fig. 3, reprinted from [75]) is about 130 μK/pixel (or about 200 μK/pixel if the M31 Bulge is excluded). This temperature asymmetry, similar in the three WMAP bands W, V and Q, is very likely induced by the Doppler shift effect due to the M31 disk rotation speed. A similar effect is clearly visible also towards the M31 halo up to about 120 kpc from the M31 center with a peak value of about 40 μK/pixel.

The robustness of this result has been tested, both for the M31 disk and halo, by considering 500 randomly distributed control fields in the three WMAP bands and also by simulating 500 sky maps (see [76] for more details). CMB maps are simulated by assuming $\Delta T(\hat{n}) = \Delta T_{CMB}(\hat{n}) \otimes B(\hat{n}) + N(\hat{n})$, where ΔT_{CMB} is a realization

of the Gaussian CMB field, $N(\hat{n})$ is the pixel noise and $B(\hat{n})$ is the proper beam of the experiment. Using the synfast routine of HEALPix[77] with the best-fit power spectrum constrained with BAO and H_0, as given by the WMAP Collaboration, 500 realizations of the CMB sky were made. The maps have been then convolved with the WMAP beams for W, V, and Q bands, respectively, taking into account the convolution with the beam function of the experiment and randomly extracting the noise value from a normal distribution with $\sigma = \sigma_0/\sqrt{N_{obs}}$. The statistical analysis shows that there is a probability below about 1% that the temperature asymmetries both in the M31 disk and halo are due to random fluctuations of the CMB signal.

The degree to which galactic halos rotate with respect to the disks is a difficult task to be investigated. In this respect, the methodology of using CMB data to probe both the disk and the halo of M31, even if with the limitation of the presently available data, may suggest a novel way of approaching this problem especially in view of the high accuracy CMB measurements with the *Planck* satellite.

5.4. *Cosmic Infrared Background anisotropies*

The Cosmic Infrared Background (CIB) is the relic emission, at wavelengths larger than a few microns, of the formation and evolution of the galaxies of all types, including Active Galactic Nuclei (AGN) and star-forming systems[78–82j]. The CIB

[j]An important goal of studies about galaxy formation has thus been the characterization of the statistical behavior of galaxies responsible for the CIB - such as the number counts, redshift distribution, mean SED, luminosity function, clustering – and their physical properties, such as the roles of star-forming vs. accreting systems, the density of star formation, and the number density of very hot stars.

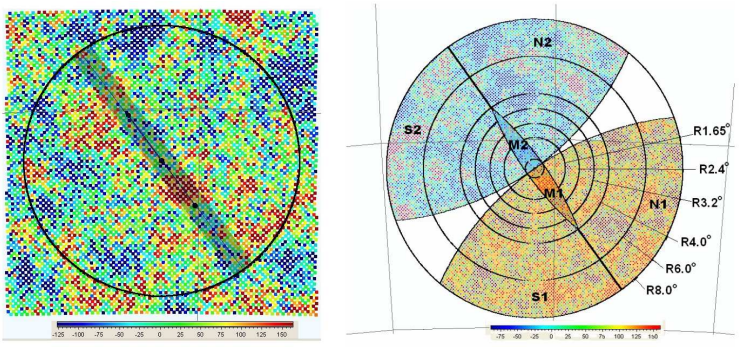

Fig. 3. The detailed geometry (up to 8°) used in the analysis is shown. The different pixel colors indicate the difference of the CMB temperature with respect to the average temperature set to zero. Red means positive excess and goes up to a maximum of 150μK while blue means lower temperature and goes up to -125μK. The left image shows the real WMAP W band map, while the right image shows the geometry used in the analysis and the average temperature in the two sides of the M31 disk and halo in false colors. It shows in a single glance that one side of both the M31 disk and halo is hotter with respect to the other side.

accounts for roughly half of the total energy in the optical/infrared Extragalactic Background Light (EBL)[81], although with some uncertainty, and its SED peaks near 150 μm. Since local galaxies give rise to an integrated infrared output that amounts to only about a third of the optical one[83], there must have been a strong evolution of galaxy properties towards enhanced far–IR output in the past. Therefore, the CIB, made up by high density, faint and distant galaxies[k] is barely resolved into its constituents. Indeed, less than 10% of the CIB is resolved by Spitzer at 160 μm[84], $\sim$ 10% by *Herschel* at 350 μm[85] and $\sim$ 16% by the SCUBA-2 Cosmology Legacy Survey (S2CLS) at 450 μm[86]. With the advent of large area far-IR to millimeter surveys (*Herschel*, *Planck*, SPT, and ACT), CIB anisotropies thus constitute a new tool for structure formation and evolution studies.

Because the clustering of dark matter is reasonably well understood, observations of anisotropies in the CIB constrain the relationship between dusty, star-forming galaxies at high redshift, i.e. $z > 2$, and the underlying dark matter distribution. The APS of CIB anisotropies has two contributions: a white-noise component caused by shot noise and an additional component caused by spatial correlations between the sources of the CIB. Correlated CIB anisotropies have already been measured by many space–borne as well as ground–based experiments (see [87] for more details). On small angular scales ($\ell \geq 2000$), they measure the clustering within a single dark matter halo and, accordingly, the physics governing how dusty, star–forming galaxies form within a halo. On larger angular scales, i.e. $200 \leq \ell \leq 2000$, CIB anisotropies measure clustering between galaxies in different dark matter halos. These measurements primarily constrain the large-scale, linear bias, b, of dusty galaxies, which is usually assumed to be scale-independent over the relevant range.

Thanks to the exceptional quality of the *Planck* data, [87] were able to measure the clustering of dusty, star-forming galaxies at 217, 353, 545, and 857 GHz with unprecedented precision. After careful cleaning, based on suitable templates and *Planck* maps, they obtained CIB anisotropy maps that reveal structures produced by the cumulative emission of high-redshift, dusty, star–forming galaxies. The power spectra of the latter maps were then computed with high signal-to-noise ratio over the range $200 < l < 2000$ by [87]. These measurements compare very well with previous measurements at higher ℓ[l]. Moreover, from *Planck* data alone [87] could exclude a model where galaxies trace the (linear theory) matter power spectrum with a scale-independent bias: that model requires an *unrealistic* high level of shot noise to match the small-scale power they observed. Consequently, an alternative model that couples the dusty galaxy, parametric evolution model of [88] with a halo model approach has been developed (see, again, [87] for more details). Characterized

[k]The CIB records much of the radiant energy released by processes of structure formation occurred since the decoupling of matter and radiation, four hundred thousand years after the Big Bang, when the CMB was produced.

[l]The SED of CIB anisotropies is not different from the CIB mean SED, even at 217 GHz. This is expected from the model of [88] and reflects the fact that the CIB intensity and anisotropies are produced by the same population of sources.

by only two parameters, this model provides an excellent fit to the measured CIB anisotropy APS for each frequency treated independently.

6. Clusters of galaxies and their cosmological implications

The observation of clusters of galaxies through the Sunyaev-Zel'dovich (SZ) effect, the inverse Compton scattering of cosmic microwave photon by hot intra-cluster electrons[89] , have proven to be an efficient way to search for new clusters[65,90,91] .

The *Planck* satellite has been observing clusters of galaxies via the measurement of the SZ effect over the whole sky since August 2009. Although, its spatial resolution is moderate with respect to ground based SZ surveys (see e.g. [65,90]), it possesses a unique nine-band coverage from 30 to 857 GHz and, most crucially, it covers an exceptionally large survey volume. Indeed *Planck* is the first all-sky survey capable of blind cluster detections since the *ROSAT* All-Sky Survey (RASS, in the X-ray domain). Early *Planck* results on galaxy clusters were recently published in [91–96]. These results include the publication of the high signal–to–noise ratio (S/N $>$ 6) Early SZ (ESZ) cluster sample[92] .

6.1. *Planck SZ clusters*

Using this specific SZ signature, *Planck* was designed to be able to detect numerous clusters[97] . Unfortunately, not all are showing up as Abell 2319. The signal is indeed quite weak and is contaminated by foregrounds (our Galaxy, and nearby radio/IR galaxies) and backgrounds (CMB and CIB). As described later, the published *Planck* clusters have a signal–to–noise ratio (S/N) greater than 6. This means that the S/N per frequency is of the order of 1. This has lead us to develop a specific approach for detecting, validating and confirming clusters.

We use a multi-matched filter (MMF) method[98] to detect the clusters. It is taking advantage of the spectral signature (SZ signature without relativistic effects) *and* the spatial signature (universal spherical profile from X-ray REXCESS observations[99]) of the clusters detected by *Planck*. As optimal as the method can be, a process of validation is still necessary to remove false detections. This is done in two steps. First a cross-check with internal *Planck* catalogues (cold cores, solar system objects, bad pixels) is performed, then cross-checks with existing external catalogues and data (SDSS, RASS) are performed to classify the known clusters and the new candidate clusters. Finally, follow-up observations has been done in optical, SZ and mainly in X-ray with XMM-Newton, to confirm our candidate clusters.

6.1.1. *Planck Early SZ cluster sample*

These detection, validation, and confirmation steps have lead to the production of the *Planck* Early SZ Cluster sample (ESZ). It contains 199 clusters, 10 of which, confirmed by XMM-Newton validation program[91,100,101] , have a S/N $<$6. The 189 clusters with S/N greater than 6 are divided in 169 known clusters (in X-ray, optical

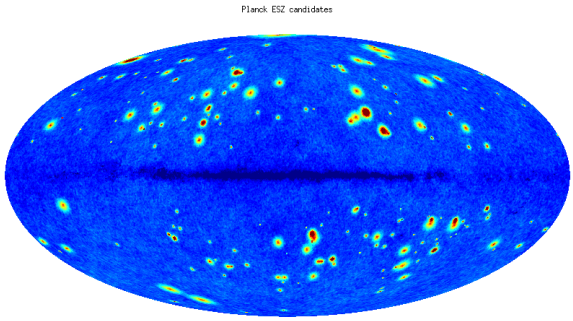

Fig. 4. Distribution on the sky of the *Planck* ESZ clusters (the signal has been amplified to be seen).

or SZ) and 20 new *Planck* clusters. At the time of the release only 11 were confirmed by XMM-Newton. Since then, 6 more have been confirmed by SPT and AMI[102,103] . The sample is available[m] as part of the *Planck* Early Release Compact Source Catalogue (ERCSC)[59] . The distribution on the sky of these clusters is shown in Fig. 4 (reprinted from [104]).

The ESZ clusters have relatively low redshift; 86% of them have $z < 0.3$. Their masses span more than a decade up to $1.5 \cdot 10^{15} M_{sol}$, and a large fraction of new *Planck* detected clusters are massive ($> 9 \cdot 10^{14} M_{sol}$). *Planck* has thus a unique capability to detect the rarest and most massive clusters over the full sky.

6.1.2. *SZ clusters properties*

Observing galaxy clusters in SZ opens a new observational window to understand the clusters themselves and the evolution of our Universe. *Planck* has detected new clusters, sometimes massive. Why have they not been detected already in X-ray? Is this a new population of clusters, or the gas (responsible for both X-ray and SZ emissions) properties differ from what we think? As massive objects, clusters are sensitive to cosmological initial conditions and cosmic evolution. To use clusters for cosmological studies we need to relate their mass to our observation (SZ effect or Y-parameter). But is SZ effect a good proxy for the mass? How does the SZ signal relates to the X-ray luminosity, to the richness of clusters? The *Planck* ESZ clusters and *Planck* data are and will help in answering these questions.

6.1.3. *New Planck clusters*

The new *Planck* confirmed clusters have been compared with REXCESS X-ray detected clusters. *Planck* clusters show a more complex morphology, being sometimes

[m] rssd.esa.int/Planck

Fig. 5. **Left panel:** *Planck* SZ and XMM X-ray images of PLCKG214.6+37.0. **Right panel:** electronic density profiles of *Planck* and REXCESS clusters.

really diffuse, extended, disturbed, and also double or triple. For the same given mass, they are also sub-luminous in X-ray compared to the REXCESS ones. Their electronic density profiles is on average lower in the center than the REXCESS ones (see Fig. 5, reprinted from [91]). Multi-wavelenght studies will help understand these properties. For example, [105] have observed one the XMM confirmed *Planck* new clusters and found radio arcs. Such findings, revealing shocks and/or merger, would imply higher temperature areas, that could enhance the SZ signal and explain why these clusters are seen in SZ and not in X-ray. More dedicated multi-wavelenght studies are thus needed to better understand these clusters.

6.2. *Baryons in clusters of galaxies as seen in the Planck survey*

The total SZ signal is closely related to the cluster mass (see e.g. [106]), and its surface brightness insensitive to distance. Therefore, SZ surveys can potentially be used to built sample of galaxies selected in mass from the local to the distant Universe (i.e., a constant mass threshold out to large redshifts). These scaling relations also bear the imprint of all gravitational and non-gravitational physical processes at play in the process of structure formation and evolution. Therefore such SZ samples of galaxy clusters will be of tremendous help for structure formation studies and to provide CMB independent cosmological constraints (see e.g. [107–109]. However, this requires a precise understanding of the statistical properties of the cluster population and furthermore a precise calibration of scaling relations between clusters physical properties and their mass. In the following, we focus on the current results on SZ scaling relations with respect to *Planck*'s results. From three different approaches, we have brought tight constraints on the scaling relations between the SZ signal and clusters physical quantities.

The statistical combination of ~ 1600 MCXC clusters at $0.01 < z < 1$ [110] with the all-sky *Planck* data led to a precise measurement of the correlation between the SZ signal and the X-ray luminosity. Averaging SZ fluxes in bins of X–ray luminosity, L_X, we detected the SZ signal at very high significance. This *Planck* observed signal is consistent with X-ray based predictions over two decades in X–ray luminosity, down to $L_X = 10^{43}\mathrm{erg/s} \lesssim L_{500}E(z)^{-7/3} \lesssim 2 \times 10^{45}\mathrm{erg/s}$. We found no deficiency

in SZ flux with respect to the X–rays within R_{500}. This results underlines the robustness and consistency of our overall view of intra-cluster medium properties (left panel of Fig. 6; reprinted from Fig. 4 in [93]). This analysis fully agrees with the similar study carried on beforehand on the WMAP-5 data by [19].

Moreover, it is also consistent with the more in-depth investigation of the local scaling relations conducted over a sample of 62 massive known clusters detected by *Planck* at a high signal-to-noise ratio and with archival *XMM-Newton* data[94] . This analysis has allowed us to investigate the scaling relations between the SZ signal, $D_{\rm A}^2\,Y_{500}$, and the X-ray-derived properties (i.e., gas mass $M_{\rm g,500}$, temperature $T_{\rm X}$, luminosity $L_{500,[0.1-2.4]\,\rm keV}$, SZ signal analogue $Y_{\rm X,500} = M_{\rm g,500} \times T_{\rm X}$, and total mass M_{500}). The derived results are in excellent agreement with both X-ray predictions and recently-published ground-based data derived from smaller samples (middle panel of Fig. 6, reprinted from Fig. 4, left panel, in [94]; see [111,112]).

Finally, as stressed in the previous section, the new clusters detected by *Planck* follow the same scaling relations out to $z = 1$ without significant deviation from self-similar evolution, exhibiting an equivalent agreement between their SZ and X-ray properties as show on the right panel of Fig. 6 (reprinted from Fig. 7 in [101]; see [93,100]). This behavior is seen down to an SZ signal of $Y_{500} \sim 3 \times 10^{-4}$ arcmin^2. Below this threshold, we reach the current detection limit of *Planck* and Malmquist bias clearly appears (for details see [101]).

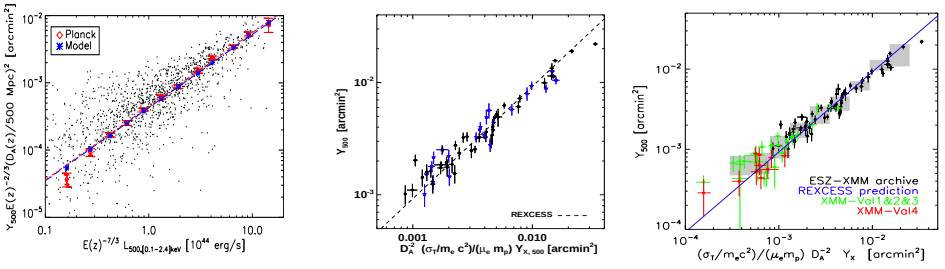

Fig. 6. **Left panel:** Scaling relation between *Planck* SZ measurements and X-ray luminosity for $\sim$ 1600 MCXC clusters. Individual measurements are shown by the black dots and the corresponding bin averaged values by the red diamonds. Thick bars give the statistical errors, while the thin bars are bootstrap uncertainties. The X-ray based model is shown as a solid blue line, and the bin-averaged SZ cluster signal it predicts is shown by the blue stars. The red dot-dashed line shows the best fitting power-law to the data. **Middle panel:** SZ flux vs prediction from X-rays. Blue stars indicate cool core systems. The dashed line is the prediction from REXCESS X-ray observations. **Right panel:** Relation between apparent SZ signal (Y_{500}) and the corresponding normalized $Y_{\rm X}$ parameter. Black points show clusters in the *Planck*-ESZ sample with *XMM-Newton* archival data; green and red points represent *Planck* clusters confirmed with *XMM-Newton* validation program. The blue lines denote the Y_{500} scaling relations predicted from the REXCESS X-ray observations. The grey area corresponds to median Y_{500} values in $Y_{\rm X}$ bins with $\pm 1\sigma$ standard deviation.

As pointed out recently by [113], some observational and/or survey biases may arise from the combination of different effects and systematic biases. On the side

of observable biased, one can mentioned the well known hydrostatic equilibrium hypothesis which biases the X-ray masses low with respect to the true mass by 10-20%[114,115]. The richness and weak lensing mass estimators from optical observations require a better control of their individual and statistical measurements[113,116–119]. Finally for SZ measurements, cross-calibration between *Planck*, SPT and ACT measurement are certainly needed to further lower the photometric uncertainties and assess possible SZ flux measurement systematics.

Some of the aforementioned biases have been investigated on an individual cluster basis in [120], where the relation between the *Planck* SZ signal and the mass was studied using total masses derived from both weak lensing (WL) measurements[121,122] and from Xray data assuming hydrostatic equilibrium (HE; *XMM-Newton* observations). While the $M_{\rm WL} - D_{\rm M}^2 Y$ relation was consistent with previous measurements using WL masses[65], there was an offset in normalization with respect to the relation obtained using HE X-ray mass measurements. Since both the SZ measurements and the HE X-ray masses were consistent with our previous work, we concluded that the normalization offset in the $M_{\rm WL} - D_{\rm M}^2 Y$ is due to the X-ray masses being ~ 20 per cent higher than the WL masses. This is an unexpected result, given that simulations generally predict that HE X-ray masses should be smaller than WL masses owing to a the neglect of pressure support from bulk gas motions in the HE mass equation. Further investigation showed that the discrepancy is enhanced in dynamically disturbed systems and appears correlated with differences in mass concentration and the offset between the X-ray peak and the BCG position (the centers used for the X-ray and Wl mass determinations, respectively). More work is clearly needed, as discussed extensively in [120]. These remaining 10-20% inconstancies in scaling relations between SZ, X-ray and optical data are at hand. They need to be further investigated and quantified in order to reach an holistic view of the galaxy cluster properties.

Together with the SPT and ACT telescopes, the *Planck* survey is shading new light on the population of galaxy clusters complementing our existing view of the ICM hot gas from the X-ray observations with high precision multi-frequency submillimeter to centimeter measurements. The scaling properties of the SZ signal together with other cluster observables have been investigated with various means and methods. Well constrained scaling relations between the SZ and X-ray measurements have been derived, with high precision calibration for the $Y_{500} - Y_{\rm X,500}$, $Y_{500} - L_{\rm X,500}$ and $Y_{500} - M$ relations. These results emphasize the well consistent picture we have of the ICM at least within R_{500}. Further *Planck* intermediate results are currently being published providing further insights on the clusters of galaxies.

6.3. *Neutrino mass from SZ surveys*

We explore here the possibility of setting useful constraints on the total neutrino mass from cluster number counts obtained by the ongoing *Planck*/SZ and future cosmic-variance-limited surveys. The precision with which this mass can be deter-

mined from SZ number counts is limited mostly by uncertainties in the cluster mass function and intra-cluster gas evolution. We find that projected *Planck*/SZ cluster counts could yield the total neutrino mass with a (1σ) uncertainty of 0.06 eV, assuming the mass is in the range $0.1 - 0.3$ eV, and the survey detection limit is set at the 5σ significance level. Based on expected results from future cosmic-variance-limited (CVL) SZ survey, we predict a 1σ uncertainty of 0.04 eV, a level comparable to that expected when CMB lensing extraction is carried out with the same experiment.

CMB measurements already placed meaningful upper limits on the total neutrino mass from its impact on the early integrated Sachs-Wolfe effect. The energy scale of recombination, ~ 0.3 eV, sets this upper limit; if the total neutrino mass is larger than this value, then neutrinos are non-relativistic and do not contribute to the decay of gravitational potentials shortly after recombination. If, on the other hand, the total mass is lower they constitute a relativistic component that contributes to the decay of linear gravitational potentials, changing the temperature of the CMB towards these gravitational wells.

Applying optimal estimators to CMB temperature and polarization maps one can recover the lensing potential to the precision that will allow constraining the total neutrino mass to the 0.04 eV level (see [123]) with a cosmic-variance-limited (CVL) CMB experiment, assuming full-sky coverage, no foregrounds, and no source of non-Gaussianity other than the lensing of the CMB. In practice, it is unlikely that all these conditions will be fully satisfied and in that sense the frequently-quoted value 0.04 eV is likely to be unrealistic.

Cluster number counts are yet another useful probe of neutrino masses. This is due to the fact that typical cluster scales are much smaller than the ~ 150 Mpc scale of linear dark matter halos that lens the CMB. In addition, cluster number counts are exponentially sensitive to $\sigma(M, z)$, the rms mass fluctuation on a cluster mass scale M at redshift z, and since $\sigma(M, z)$ itself is exponentially sensitive to neutrino mass (via the growth function), this implies that cluster number counts should be a rather sensitive probe of neutrino masses (see e.g. [124,125]).

We further explored the ability to strengthen the constraints on the neutrino mass from cluster number counts, and extended our forecast to additional surveys. This was done by parameterizing uncertainties in the halo mass function, which is the dominant source of modeling uncertainties. The shape and normalization of the mass function reflect the details of the growth of density fluctuations, and the nonlinear collapse and merger of sub-structures, whose hierarchical evolution can be best studied by state-of-the-art, large-volume hydrodynamical cosmological simulations. Currently available numerical codes predict a range of mass functions; this indeterminacy largely sets the precision limit of forecasting the total neutrino mass from cluster SZ number counts and power spectra. Additionally, we have accounted for cluster sample variance errors (in addition to Poissonian noise), a more realistic intra-cluster gas profile, as well as gas evolution with cluster mass and redshift. A full description of this work and results is given by]126].

Our analysis shows that from cluster number counts alone (and priors based on measurements of the primary CMB APS and the HST prior on H_0), the uncertainty in the determination of the total neutrino mass can be limited to the $\sim 0.04 - 0.06$ eV range, depending on the details of the SZ cluster surveys and the fiducial neutrino mass. CMB anisotropy data combined with *Planck* cluster number counts are predicted to reach a level uncertainty at the higher end of this interval, whereas a CVL SZ survey is predicted to yield the somewhat higher precision corresponding to the lower end of this mass uncertainty interval. These results are based on the mass function by [127], whose parameter values were assumed to have uncertainties that are higher by 10% than those specified there.

7. Selected topics in CMB studies

The release of first cosmological products and papers from the *Planck* mission, waited for early 2013, will have a strong impact for cosmology in the coming decades, following the very important results from WMAP and recent ground-based projects together covering a wide multipole range. In this section we discuss three very different topics: the first is connected to fundamental physics results expected in next times from the *Planck* mission; the second, regarding the polarization imprints induced by galaxy clusters and filaments, is relevant in particular for future high resolution ground-based experiments; the last concerns the information on primordial power spectrum at extremely high wavenumbers that could be derived from next generations of CMB spectrum missions, thus linking absolute measures of the CMB monopole, i.e. the largest angular scale, to small scale phenomena.

7.1. *Fundamental physics from CMB Parity analyses*

The statistical properties of the CMB pattern may be used to constrain Parity (P) symmetry. Parity violations arise in several models: as modification of electromagnetism[128–130] or as modification of the standard picture of the Inflationary mechanism, where P is broken due to primordial (chiral) gravitational waves[131–133] . Both of these scenarios predict non null cross-correlations between gradient and curl modes and scalar and curl modes in the CMB polarization pattern. However, chiral gravity induces such correlations at the CMB last scattering surface whereas cosmological birefringence induces them by rotating the polarization plane during the CMB photon journey from its last scattering to us[134] . We focus here mainly on cosmic birefringence, reporting findings from Gruppuso et al. 2011[135] . In addition, we discuss the claimed P anomaly found at large angular scales in the anisotropy intensity spectrum of the WMAP data, first claimed by Kim and Naselsky in 2010[136–139] . The latter is dubbed a parity anomaly in view of an observed discrepancy (in power) among even and odd multipoles, which behave differently under P transformation. However, there is no sound theoretical framework that could explain such a mismatch. If the effect is indeed due to fundamental physics, its appearance at large angular scales naturally suggests the possibility that a P violating mechanism is

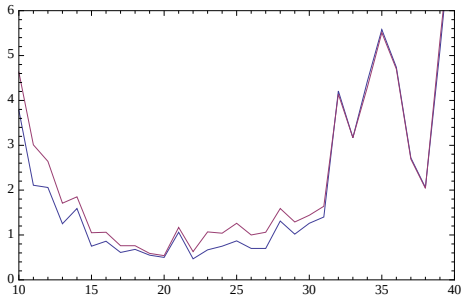

Fig. 7. TT. Percentage of the WMAP 7 year value (y-axis) vs ℓ_{max} (x-axis). Blue line is for the ratio and the red line for the difference.

involved during an early phase of the universe. Other explanations exist: for a more conservative approach see [137] where it is conjectured that we may live in a special location of the universe, such that translational invariance is violated at scales larger than ~ 4 Gpc.

7.1.1. *TT Parity anomaly*

All-sky temperature maps, $T(\hat{n})$, are usually expanded in terms of spherical harmonics $Y_{\ell m}(\hat{n})$, with $\hat{n}$ being a unit vector or direction on the sky, completely specified by a couple of angles (θ, ϕ). The quantities $a_{T,\ell m} = \int d\Omega\, Y^{\star}_{\ell m}(\hat{n})\, T(\hat{n})$, are coefficients of the SH expansion, and $d\Omega = d\theta d\phi \sin\theta$. Under reflection (or P) symmetry ($\hat{n} \to -\hat{n}$), these coefficients behave as $a_{T,\ell m} \to (-1)^{\ell}\, a_{T,\ell m}$. CMB physics does not distinguish between even and odd multipoles[136,137]. Therefore the power contained in even and odd multipoles must be statistically the same. We thus define the quantity:

$$C^X_{+/-} \equiv \frac{1}{(\ell_{max}-1)} \sum_{\ell=2,\ell_{max}}^{+/-} \frac{\ell(\ell+1)}{2\pi}\, \hat{C}^X_{\ell} \tag{8}$$

where $\hat{C}^X_{\ell}$ are power spectral estimates for X = TT, TE, EE and BB. The sum is meant only over the even or odd ℓ and this is represented respectively by the symbol + or −. Therefore, two estimators can be built from Eq. (8): the "ratio" $R^X = C^X_+/C^X_-$ (see [136–138]) and the "difference" $D^X = C^X_+ - C^X_-$ (see [138,140]), where $C^X_{\pm}$ is the band power average contained in the even (+) or odd (-) multipoles. In Fig. 7 (reprinted from [135]) we plot the percentage related to the WMAP 7 year P anomaly for TT versus ℓ_{max} in the range $10-40$ for the two considered estimators. As evident there is not a single ℓ_{max} for which the TT anomaly shows up, but rather a characteristic scale in the ℓ range $[15, 25]$. We confirm the previously reported P anomaly in TT in the range $\Delta\ell = [2, 22]$ at $> 99.5\%$ C.L.. *Planck* will not improve the signal-to-noise ratio in this range for the TT APS, since it is already cosmic variance dominated in the WMAP data. However, *Planck* has a wider frequency coverage and this will improve the component separation layer in the data analysis

pipeline. Moreover, *Planck* is observing the sky with a totally different scanning strategy and this represents a benefit for the analysis of systematic effects.

7.1.2. *Cosmological birefringence*

Linear polarization maps are components of a rank two tensor[141] and are decomposed by the spin harmonics $a_{\pm2,\ell m} = \int d\Omega\, Y^{\star}_{\pm2,\ell m}(\hat{n})\,(Q(\hat{n}) \pm iU(\hat{n}))$, where $Y_{\pm2,\ell m}(\hat{n})$ are SH of spin 2 and $a_{\pm2,\ell m}$ are the corresponding coefficients. It is then useful to introduce new coefficients as linear combinations of the previous: $a_{E,\ell m} = -(a_{2,\ell m}+a_{-2,\ell m})/2$ and $a_{B,\ell m} = -(a_{2,\ell m}-a_{-2,\ell m})/2i$. These have opposite behaviors under a P transformation: $a_{E,\ell m} \to (-1)^{\ell}\, a_{E,\ell m}$, $a_{B,\ell m} \to (-1)^{\ell+1}\, a_{B,\ell m}$. If P is conserved, by combining the previous transformation one immediately derives that the cross-correlations $C_{\ell}^{TB} = \langle a^{\star}_{T,\ell m} a_{B,\ell' m'} \rangle$ and $C_{\ell}^{EB} = \langle a^{\star}_{E,\ell m} a_{B,\ell' m'} \rangle$ must vanish. Further details can be found in [141,142] and explicit algebra is set forth in the Appendix of [138]. Parity violation could, however, may change this scenario. A popular model for which parity is broken in the photon sector is the Chern-Simons perturbation to the Maxwell Lagrangian[128]: $\Delta\mathcal{L} = -\frac{1}{4}\, p_{\mu} \epsilon^{\mu\nu\rho\sigma} F_{\rho\sigma} A_{\nu}$, where $F^{\mu\nu}$ is the Maxwell tensor and A^{μ} the four-potential. One of the consequences is in vacuo dispersion of photons, in particular those from the CMB and the rotation of their polarization planes, observable through TB and EB correlations, that acquire a signal modulated by α (or "rotated")[131,143–146].

The WMAP team[147] reported $\alpha^{\mathrm{WMAP\,7yr}} = -0.9^{\circ} \pm 1.4^{\circ}$ at 68% C.L.. Our constraint, obtained at low resolution[135] and considering the same estimator that has been used in [148], reads $\alpha = -1.6^{\circ} \pm 1.7^{\circ}\,(3.4^{\circ})$ at 68% (95%) C.L. for $\Delta\ell = 2 - 47$. Considering $\Delta\ell = 2 - 23$ we obtain $\alpha = -3.0^{\circ}{}^{+2.6^{\circ}}_{-2.5^{\circ}}$ at 68% C.L. and $\alpha = -3.0^{\circ}{}^{+6.9^{\circ}}_{-4.7^{\circ}}$ at 95% C.L.. This is the same multipole range considered by the WMAP team at low resolution in [147] (the only other result available in the literature at these large angular scales) where with a pixel based likelihood analysis they obtain $\alpha^{\mathrm{WMAP\,7yr}} = -3.8^{\circ} \pm 5.2^{\circ}$ at 68% C.L.. In [149] it is claimed that the improvement expected for the *Planck* satellite[5] in terms of sensitivity[150] is around 15. Almost the same number is obtained in Gruppuso et al. [135]. Both forecasts are provided considering just the nominal sensitivity whereas the uncertainties coming from the systematic effects are not taken into account.

7.2. *CMB induced polarization from single scattering by clusters of galaxies and filaments*

We discuss here two types of secondary polarization effects arising from single scattering of the CMB photons by ionized gas. These are the CMB quadrupole induced polarization (pqiCMB), which couples the gas density with the CMB quadrupole component, and the polarization induced by the gas motion transverse to the line of sight (pβ_t^2SZ).

Instead of using an analytical model adopted in many previous studies or simulations of individual galaxy clusters (see e.g. [151–154]), we used high-resolution

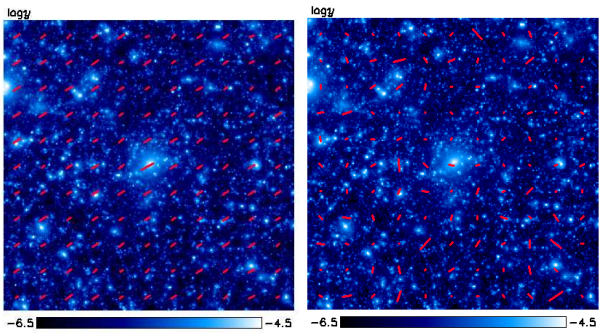

Fig. 8. Polarization map (red vectors) of $0.93^\circ \times 0.93^\circ$ integrated in redshift of one sky patch realization for pqiCMB (left panel) and pβ_t^2SZ (right panel). For comparison, we put the logarithm of Compton y-parameter (color scaled).

N-body/Hydrodynamic simulations featuring adiabatic gas physics and a novel box-stacking scheme that allows to reconstruct the CMB quadruple component and the physical properties of the scattering media along the light cone traversed by radiation. We generated 28 random sky patches integrated along the light-cone, each of about 0.86 deg^2 at angular resolution of 6". The primordial CMB quadrupole information in each simulation box is computed by inverse Fourier transform of CMB quadrupole components in Fourier space at all conformal times required by the map-making strategy. For each individual Fourier mode, we decide the initial value $\Psi_i(\mathbf{k})$ by drawing a random number from a Gaussian distribution with variance given by the initial power spectrum obeys a power law, $P_\Psi(k) = Ak^{n_s-4}$ with A a normalization factor and n_s a spectral index of the scalar perturbations. The time evolution of CMB quadrupole in each individual mode is computed using the CMBFast[155] Boltzmann code (see [156] for more details). Here we focus on the characterization of the polarized signals in the simulations and the study of their statistical properties at high angular resolution.

The results from the pixel distribution in the frequency independent maps, show that the linear polarization degrees follows, in logarithm scale, nearly Gaussian distributions, centered around 10^{-8} and 10^{-10} for pqiCMB and pβ_t^2SZ, respectively. Our simulations confirm that the polarization degree of the pqiCMB is a close proxy of the electron density column and that the polarization angles of this effect are closely aligned due to the slow variation of primary CMB quadrupole on small sky patches and along the line of sight (see Fig. 8, reprinted from [156], left panel). The effect of the gas overlap along density columns causes galaxy clusters and other bound objects to be less prominent (with respect to the mean background) than in the case of the thermal SZ effect, where the signal in clusters is boosted by the high temperature. In the case of pβ_t^2SZ (right panel of Fig. 8), the polarization degrees and angles are weighted by the transverse velocity of the scattering media, therefore the integration along the line of sight can erase contributions from individual

collapsed objects, depending on their internal velocity structure and the effect of gas overlap.

By producing maps of these secondary induced polarization effects at different frequencies, we confirm the strong dependence on frequency of both signals, especially in the case of pβ_t^2SZ, for which the mean value increases by a factor of ~ 100 from the 30 GHz to 675 GHz. The high magnitudes of both signals at high frequencies may allow its detection with the next generation of sub-millimeter instruments.

The redshift distribution of the polarization degrees shows that the contribution for the polarization signal is highest at $z \simeq 1$ and $z \simeq 0.5$ for the pqiCMB and pβ_t^2SZ, respectively. Finally, only about 7% of the total signal comes from $z > 4$ for the former and $z > 3$ for the latter and both signals converge rapidly at larger z.

7.3. *Mixing of blackbodies: creation of entropy and dissipation of sound waves in the early Universe*

There is a very important connection between the spectrum of the monopole or sky averaged CMB, which is an almost perfect blackbody and COBE/FIRAS[157] detected no deviation from Planck spectrum, and the angular anisotropies precisely measured by WMAP[158] , SPT[159] , ACT[160] , *Planck* and other experiments on scales corresponding to comoving wavenumber $10^{-4} \lesssim k \lesssim 0.2$ Mpc^{-1}, including the damping tail due to photon diffusion[161,162] . The power that disappears from the CMB APS because of Silk damping appears in the energy spectrum of monopole as y[163] , μ and intermediate-type distortions[164,165] . The primordial power spectrum, at comoving wavenumbers $8 \lesssim k \lesssim 10^4$ Mpc^{-1} (mostly inaccessible by any other means), can thus be recovered by precise measurements of the energy spectrum of the monopole.

The current constraints on the primordial power spectrum, including Ly-α forest constraints[166,167] , are shown in the left panel of Fig. 9 (reprinted from [165]). At present the small-scale constraints from COBE/FIRAS y-type (2σ limit $y \lesssim 1.5 \times 10^{-5}$) and μ-type ($\mu \lesssim 9 \times 10^{-4}$) distortions are very weak and considerable freedom is allowed on small scales. Proposed future experiment PIXIE[168] would improve the small-scale constraints by a factor of ~ 2500 and start probing the interesting region of the parameter space, extending our knowledge of the primordial power spectrum by many orders of magnitude in terms of the scales probed.

Previous calculations of spectral distortions in CMB from Silk damping[169–171] underestimated the energy in sound waves and also assumed that all the dissipated energy goes into creating spectral distortions. The physics of creation of spectral distortion becomes very simple if we consider the fact that diffusion of photons, which damps the CMB perturbations, is in fact mixing blackbodies of different temperature[172,173] . The right panel in Fig. 9 (reprinted from [173]) shows the result of averaging two blackbodies with temperatures $T \pm \Delta T$. The resulting spectrum is marked 'Average(Y)' and is a y-type distortion[174] on top of a blackbody with temperature $T\left[1 + (\Delta T/T)^2\right]$ with the two curves crossing at $x = 3.83$. The averaging

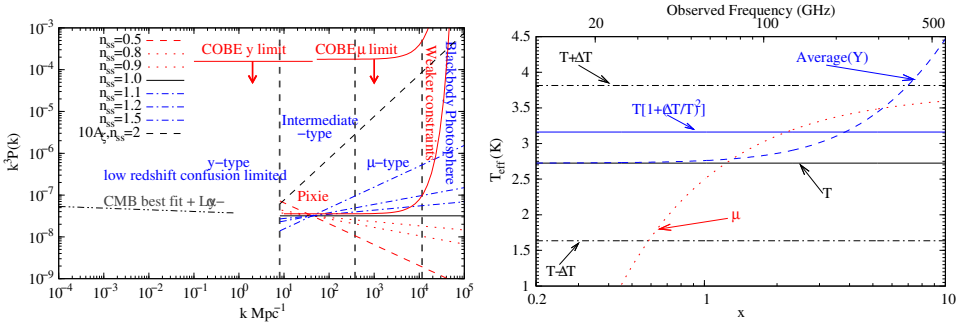

Fig. 9. **Left panel:** current and future constraints on primordial power spectrum as a function of comoving wavenumber k. Possible spectra on small scales allowed by current data are also shown. **Right panel:** the spectrum resulting from mixing of blackbodies. We have used the linear (in $(\Delta T/T)^2$) solution to make the plots but used a large value of $\Delta T/T$ to make the differences visible. Effective temperature of the spectrum defined by writing the occupation number as $n = 1/(e^{h\nu/(k_{\rm B}T_{\rm eff})} - 1)$ as a function of dimensionless frequency, $x = h\nu/kT$ is plotted. At high redshifts, $z \gtrsim 10^5$, the spectrum comptonizes rapidly to create a μ-type distortion or Bose-Einstein spectrum, also shown in the figure.

of two blackbodies adds energy as well as photons to the average CMB monopole and therefore not all the energy can be used to create spectral distortions. It is straightforward to show, by using Taylor series expansion of the initial blackbodies up to second order in $\Delta T/T$ and then doing the ensemble average, that only 1/3 of the dissipated energy goes into y/μ-type distortions[173] and 2/3 just raises the temperature. Applying the above procedure to CMB immediately gives us the rate of energy injection into CMB and the resulting μ distortion[175] ,

$$\left.\frac{{\rm d}\mu}{{\rm d}t}\right|_{\rm distortion} = 1.4\,\frac{\rm d}{{\rm d}t}\left.\frac{\Delta E}{E_\gamma}\right|_{\rm distortion} = -1.4\frac{\rm d}{{\rm d}t}\frac{1}{3}6\int\frac{k^2{\rm d}k}{2\pi^2}P_i(k)\left[\sum_{\ell=0}^{\infty}(2\ell+1)\Theta_\ell^2(k)\right]$$
$$\approx -\frac{\rm d}{{\rm d}t}2.8\int\frac{k^2{\rm d}k}{2\pi^2}P_i(k)\left[\Theta_0^2+3\Theta_1^2\right], \qquad (9)$$

where $\frac{\Delta E}{E_\gamma}$ is the fractional energy going into CMB distortion, Θ_ℓ are the multipole moments of CMB temperature perturbation transfer function, P_i is the initial power spectrum, and in the second line we have used the fact that during tight coupling the $\ell \geq 2$ modes are suppressed. The time derivatives are easily calculated using the tight coupling solutions with Silk damping or by using the first order Boltzmann equation. A nice feature of the approach presented above is that the energy injected into the distortion can be directly identified with the increase in entropy of CMB[173] .

Acknowledgements – We thank the Editorial Board of Astronomy and Astrophysics (European Southern Observatory; ESO) and the Editors of the Annual meeting of the French Society of Astronomy and Astrophysics for having granted us the permission to reproduce many figures originally published (or in press) in the same Journals or Proceedings. Some figures are reproduced by permission of the AAS (American Astronomical

Society). Credits are indicated when each reprinted figure is mentioned in the text for the first time. The authors that are members of the *Planck* Collaboration warmly thank the *Planck* Collaboration and, in particular, all the members of the *Planck* Working Groups 2, 5, 6, 7 and of the HFI and LFI Core Teams, with whom they shared the analysis and the interpretation of *Planck* data as for the subjects discussed here, and the members of the *Planck* Science Team and Editorial Board for the permission of publishing this paper. CB and PN wish to thank A. Gruppuso and N. Mandolesi, with whom have carried out part of the work described in this paper. Some of the results in this paper have been derived using the HEALPIX[77] package. We acknowledge the use of the Legacy Archive for Microwave Background Data Analysis (LAMBDA) supported by the NASA Office of Space Science. Some of the simulations presented in this work have been performed using the computational facility of IASF Bologna and at CINECA. CB, MM, AM, PN acknowledge support by ASI through ASI/INAF Agreement I/072/09/0 for the Planck LFI Activity of Phase E2 and by MIUR through PRIN 2009 grant n. 2009XZ54H2. EP acknowledges the support of ANR project Multiverse under grant ANR-11-BD56-015. LT acknowledges partial financial support from the Spanish Ministerio de Economía y Competitividad, under proyects AYA2010-21766-C03-01, AYA2012-39475-C02-01 and by the Consolider Ingenio-2010 Programme, project CSD2010-00064.

References

1. A. Mennella, R.C. Butler, A. Curto, et al., *Astron. and Astrophys.* **536**, A3:1 (2011).
2. *Planck* HFI Core Team; P. A. R. Ade, N. Aghanim, et al., *Astron. and Astrophys.* **536**, A4:1 (2011).
3. A. Zacchei, D. Maino, C. Baccigalupi, et al., *Astron. and Astrophys.* **536**, A5:1 (2011).
4. *Planck* HFI Core Team; P. A. R. Ade, N. Aghanim, et al., *Astron. and Astrophys.* **536**, A6:1 (2011).
5. *Planck* Collaboration. I. P. A. R. Ade, N. Aghanim, et al., *Astron. and Astrophys.* **536**, A1: 1 (2011).
6. J. A. Tauber, H. U. Norgaard-Nielsen, P. A. R. Ade, et al., *Astron. and Astrophys.* **520**, A2 (2010).
7. M. Bersanelli, N. Mandolesi, R. C. Butler, et al., *Astron. and Astrophys.* **520**, A4:1 (2010).
8. J.-M. Lamarre, J.-L. Puget, P. A. R. Ade, et al., *Astron. and Astrophys.* **520**, A9:1 (2010).
9. M. Sandri, F. Villa, M. Bersanelli, et al., *Astron. and Astrophys.* **520**, A7:1 (2010).
10. B. Maffei, F. Noviello, J. A. Murphy, et al., *Astron. and Astrophys.* **520**, A12:1 (2010).
11. H. Kurki-Suonio, E. Keihänen, R. Keskitalo, et al., *Astron. and Astrophys.* **506**, 1511 (2009).
12. J. P. Leahy, M. Bersanelli, O. D'Arcangelo, et al., *Astron. and Astrophys.* **520**, A8:1 (2010).
13. C. L. Bennett, R. S. Hill, G. Hinshaw, et al. *The Astrophys. J. Suppl.* **148**, 97 (2003).
14. J. Dunkley, R. Hlozek, J. Sievers, et al., *The Astrophys. J.* **739**, 52 (2011).
15. N. R. Hall, R. Keisler, L. Knox, et al., *The Astrophys J.* **718**, 632 (2010).
16. F.-R. Bouchet and R. Gispert, *New Astronomy*, **4**, 443 (1999).
17. J. Delabrouille and J.F. Cardoso, *Data Analysis in Cosmology* **665**, 159 (2009).
18. S. M. Leach, J.-F. Cardoso, C. Baccigalupi, et al., *Astron. and Astrophys.* **491**, 597 (2008).

19. J.-B. Melin, N. Aghanim, M. Bartelmann, et al., *Astron. and Astrophys.* **548**, A51:1 (2012).
20. J. Delabrouille, M. Betoule, J.-B. Melin, et al., arXiv://1207.3675 (2012).
21. C. Baccigalupi, L. Bedini, C. Burigana, et al., *Mon. Not. R. Astron. Soc.* **318**, 769 (2000).
22. D. Maino, A. Farusi, C. Baccigalupi, et al., *Mon. Not. R. Astron. Soc.* **334**, 53 (2002).
23. J.-F. Cardoso, M. Le Jeune, J. Delabrouille, M. Betoule and G. Patanchon, *IEEE Journal of Selected Topics in Signal Processing* **2**, 735 (2008).
24. J. Delabrouille, J.-F. Cardoso and G. Patanchon, *Mon. Not. R. Astron. Soc.* **346** 1089 (2003).
25. G. Patanchon, J.-F. Cardoso, J. Delabrouille and P. Vielva, *Mon. Not. R. Astron. Soc.* bf 364, 1185 (2005).
26. M. Betoule, E. Pierpaoli, J. Delabrouille, M. Le Jeune and J.-F. Cardoso, *Astron. and Astrophys.* **503**, 691 (2009).
27. A. Bonaldi, L. Bedini, E. Salerno, C. Baccigalupi and G. de Zotti, *Mon. Not. R. Astron. Soc.* **373**, 271 (2006).
28. H. U. Nørgaard-Nielsen and H. E. Jørgensen, *Astrophys. Space Sci.* **318**, 195 (2008).
29. H. U. Nørgaard-Nielsen and K. Hebert, *Astronomische Nachrichten*, **330**, 863 (2009).
30. H. U. Nørgaard-Nielsen, *Astron. and Astrophys.* **520**, A87:1 (2010).
31. H. K. Eriksen, C. Dickinson, C. R. Lawrence, et al., *The Astrophys. J.* bf 641, 665 (2006).
32. R. Stompor, S. Leach, F. Stivoli and C. Baccigalupi, *Mon. Not. R. Astron. Soc.* **392**, 216 (2009).
33. J. Bobin, Y. Moudden, J.-L. Starck, J. Fadili and N. Aghanim, *Statistical Methodology*, **5**, 307 (2008).
34. J. Bobin, J.-L. Starck, F. Sureau and S. Basak, arXiv://1206.1773 (2012).
35. C. L. Bennett, G. F. Smoot, G. Hinshaw, et al., *The Astrophys J. Lett.* **396**, L7 (1992).
36. G. Hinshaw, M. R. Nolta, C. L. Bennett, et al., *The Astrophys. J. Suppl* **170**, 288 (2007).
37. S. Basak and J. Delabrouille, *Mon. Not. R. Astron. Soc.* **419**, 1163 (2012).
38. J. Delabrouille, J.-F. Cardoso, M. Le Jeune, et al., *Astron. and Astrophys.* **493**, 835 (2009).
39. C.-G. Park, C. Park and J. R. Gott III, *The Astrophys, J.* **660**, 959 (2007).
40. M. Tegmark, A. de Oliveira-Costa and A. J. Hamilton, *Phys. Rev. D* **68**, 123523 (2003).
41. M. Remazeilles, J. Delabrouille and J.-F. Cardoso, *Mon. Not. R. Astron. Soc.* **410**, 2481 (2011).
42. M. Remazeilles, J. Delabrouille and J.-F. Cardoso, *Mon. Not. R. Astron. Soc.* **418**, 467 (2011).
43. J. Dick, M. Remazeilles and J. Delabrouille, *Mon. Not. R. Astron. Soc.* **401**, 1602 (2010).
44. T. Kelsall, J.T. Weiland, B.A. Franz, et al., *The Astrophys. J.* **508**, 44 (1998).
45. D.J. Fixsen and E. Dwek, *The Astrophys. J.* **578**, 1009 (2002).
46. M. Maris, C. Burigana and S. Fogliani, *Astron. and Astrophys.*, **452**, 685 (2006).
47. M. Maris, C. Burigana, A. Gruppuso, F. Finelli and J.-M. Diego, *Mon. Not. R. Astron. Soc.* **415**, 2546 (2011).
48. M. Hansen, J. Kim, A.M. Frejsel, et al., *J. Cosmology and Astrop. Physics* **1210**, 059 (2012).
49. A. Broadbent, J. L. Osborne and C. G. T. Haslam, *Mon. Not. R. Astron. Soc.* **237**, 381 (1989).

50. B. Gold, N. Odegard, J. L. Weiland, R. S. Hill, A. Kogut, C. L. Bennett, G. Hinshaw, X. Chen, J. Dunkley, M. Halpern, N. Jarosik, E. Komatsu, D. Larson, M. Limon, S. S. Meyer, M. R. Nolta, L. Page, K. M. Smith, D. N. Spergel, G. S. Tucker, E. Wollack and E. L. Wright, *The Astrophys. J. Suppl.* **192**, 15 (2011).
51. C. Dickinson, R. D. Davies and R. J. Davis, *Mon. Not. R. Astron. Soc.* **341**, 369 (2003).
52. M. I. R. Alves, R. D. Davies, C. Dickinson, R. J. Davis, R. R. Auld, M. Calabretta and L. Staveley-Smith, *Mon. Not. R. Astron. Soc.* **405**, 1654 (2010).
53. M. I. R. Alves, R. D. Davies, C. Dickinson, M. Calabretta, R. Davis and L. Staveley-Smith, *Mon. Not. R. Astron. Soc.* **422**, 2429 (2012).
54. B. T. Draine and A. Lazarian, *The Astrophys. J. Lett.* **494**, L19 (1998).
55. *Planck* Collaboration. XX, *Astron. and Astrophys.* **536**, A20:1 (2011).
56. *Planck* Collaboration. XIX, *Astron. and Astrophys.* **536**, A19:1 (2011).
57. *Planck* Collaboration. IX *Astron. and Astrophys.* in press, arXiv://1208.5483v1 (2013).
58. E. Carretti, R. M. Crocker, L. Staveley-Smith, et al., *Nature* **493**, 66 (2012).
59. *Planck* Collaboration. VII, *Astron. and Astrophys.* **536**, A7:1 (2011).
60. M. Massardi, R.D. Ekers, T. Murphy, et al., *Mon. Not. R. Astron. Soc.* **384**, 775 (2008).
61. C.M. Urry and P. Padovani, *Pub. Astron. Soc. Pac.* **107**, 803 (1995).
62. L. Toffolatti, F. Argüeso, G. de Zotti, et al., *Mon. Not. R. Astron. Soc.* **297**, 117 (1998).
63. G. de Zotti, R. Ricci, D. Mesa, et al., *Astron. and Astrophys.* **431**, 893 (2005).
64. J. Vieira, T.M. Crawford, E.R. Switzer, et al., *The Astrophys. J.* **719**, 763 (2010).
65. T.A. Marriage, J.B. Juin, Y. Lin, et al., *The Astrophys. J.* **731**, A100:1 (2011).
66. *Planck* Collaboration. XIII, *Astron. and Astrophys.* **536**, A13:1 (2011).
67. E.L. Wright, et al., *The Astrophys. J. Suppl.* **180**, 283 (2009).
68. M. Tucci, L. Toffolatti, G. de Zotti and E. Martínez-González, *Astron. and Astrophys.* **533**, A57:1 (2011).
69. A. Königl, *The Astrophys. J.* **243**, 700 (1981).
70. A.P. Marscher, *Energy transport in radio galaxies and quasars*, A.S.P. Conf. Series, eds. P.E. Hardee, A.H. Bridle and J.A. Zensus (San Francisco: Astronomical Society of the Pacific), **100**, 45 (1996).
71. A.P. Marscher and W.K. Gear, *The Astrophys. J.* **298**, 114 (1985).
72. *Planck* Collaboration. XVI, *Astron. and Astrophys.* **536**, A16:1 (2011).
73. *Planck* Collaboration. VII, *Astron. and Astrophys.* in press, arXiv://1207.4706v1 (2013).
74. V. G. Gurzadyan, A. L. Kashin, H. G. Khachatryan, et al., *Europhysics Letters* **91**, 19001 (2010).
75. F. De Paolis, et al., *Astron. and Astrophys.* **534**, L8 (2011).
76. F. De Paolis, et al., Proc. *Thirteenth Marcel Grossman Meeting on General Relativity*, edited by R.T. Jantzen, K. Rosquist and R. Ruffini (World Scientific, Singapore, 2014).
77. K.M. Gorski, E. Hivon, A.J. Banday, B.D. Wandelt, F.K. Hansen, M. Reinecke and M. Bartelmann, *Astrophys. J.* **622**, 759 (2005).
78. J.-L. Puget, A. Abergel, J.-P. Bernard, et al., *Astron. and Astrophys.* **308**, L5 (1996).
79. C. Burigana, L. Danese, G. de Zotti, A. Franceschini, P. Mazzei and L. Toffolatti, *Mon. Not. R. Astron. Soc.* **287**, L17 (1997).
80. C. Burigana and L. Popa, *Astron. and Astrophys.* **334**, 420 (1998).
81. M.G. Hauser and E. Dwek *Ann. Rev. of Astron. and Astrophys.* **39**, 249 (2001).
82. H. Dole, G. Lagache, J.-L. Puget, et al., *Astron. and Astrophys.* **451**, 417 (2006).
83. B.T. Soifer G. and Neugebauer, *The Astron. J.* **101**, 354 (1991).

84. M. Bethermin, H. Dole, M. Cousin and N. Bavouzet *Astron. and Astrophys.* **516**, A43:1 (2010).
85. S.-J. Oliver, L. Wang, A.-J. Smith, et al., *Astron. and Astrophys.* **518**, L21 (2010).
86. J.E. Geach, E.L. Chapin, K.E.K. Coppin, et al., *Mon. Not. R. Astron. Soc.*, submitted, arXiv://1211.6668v1 (2012).
87. *Planck* Collaboration. XVIII. *Astron. and Astrophys.* **536**, A18:1 (2011).
88. M. Bethermin, H. Dole, G. Lagache G., D. Le Borgne and A. Penin, *Astron. and Astrophys.* **529**, A4:1 (2011).
89. R. A. Sunyaev and Y. B. Zel'dovich, *Comments on Astrophysics and Space Physics* **4**, 173 (1972).
90. J. E. Carlstrom, P. A. R. Ade, K. A. Aird, et al., *Publ. Astron. Soc. Pac.* **123**, 568 (2011).
91. *Planck* Collaboration. IX. *Astron. and Astrophys.* **536**, A9:1 (2011).
92. *Planck* Collaboration. VIII. *Astron. and Astrophys.* **536**, A8:1 (2011).
93. *Planck* Collaboration. X. *Astron. and Astrophys.* **536**, A10:1 (2011).
94. *Planck* Collaboration. XI. *Astron. and Astrophys.* **536**, A11:1 (2011).
95. *Planck* Collaboration. XII. *Astron. and Astrophys.* **536**, A12:1 (2011).
96. *Planck* Collaboration. XXVI. *Astron. and Astrophys.* **536**, A26:1 (2011).
97. N. Aghanim, A. de Luca, F. R. Bouchet, R. Gispert and J. L. Puget, *Astron. and Astrophys.* **325**, 9 (1997).
98. J.-B. Melin, J. G. Bartlett and J. Delabrouille, *Astron. and Astrophys.* **459**, 341 (2006).
99. M. Arnaud, G. W. Pratt, R. Piffaretti, R., et al., *Astron. and Astrophys.* **517**, A92:1 (2010).
100. *Planck* Collaboration. I. *Astron. and Astrophys.* **543**, A102:1 (2012).
101. *Planck* Collaboration. IV. *Astron. and Astrophys.*, in press, arXiv://1205.3376 (2012).
102. K. Story, K. A. Aird, K. Andersson, et al., *The Astrophys. J. Lett.* **735**, L36 (2011).
103. AMI Consortium, N. Hurley-Walker, M. L. Brown, et al., *Mon. Not. R. Astron. Soc.* **414**, L75 (2011).
104. M. Douspis, *Planck* SZ clusters, in SF2A-2011: *Proc. of the Annual meeting of the French Society of Astronomy and Astrophysics*, eds. G. Alecian, K. Belkacem, R. Samadi and D. Valls-Gabaud (2011), pp. 21-26.
105. J. Bagchi, S. K. Sirothia, N. Werner, et al., *The Astrophys. J. Lett.* **736**, L8 (2011).
106. A. C. da Silva, S. T. Kay, A. R. Liddle and P. Thomas, *Mon. Not. R. Astron. Soc.* **348**, 1401 (2004).
107. N. Sehgal, H. Trac, V. Acquaviva, et al., *The Astrophys J.* **732**, 44 (2011).
108. B. A. Benson, T. de Haan, J. P. Dudley, et al., *The Astrophys. J.*, submitted, arXiv://1211.5435 (2011).
109. C. L. Reichardt, B. Stalder, L. E. Bleem, et al., *The Astrophys. J.*, submitted, arXiv://1203.5775 (2012).
110. R. Piffaretti, M. Arnaud, G. W. Pratt, E. Pointecouteau, E. and J.-B. Melin, *Astron. and Astrophys.* **534**, A109+ (2011).
111. K. Andersson, B. A. Benson, P. A. R. Ade, et al., *The astrophys. J.* **738**, 48 (2011).
112. C. Sifon, F. Menanteau, M. Hasselfield, et al., *The Astrophys. J.*, submitted, arXiv://1201.0991 (2012).
113. R. E. Angulo, V. Springel, S. D. M. White, et al., *Mon. Not. R. Astron. Soc.* **426**, 2046 (2012).
114. S. T. Kay, P. A. Thomas, A. Jenkins and F. R. Pearce, *Mon. Not. R. Astron. Soc.*, **355**, 1091 (2004).
115. R. Piffaretti and R. Valdarnini, *Astron. and Astrophys.* **491**, 71 (2008).

116. T. Biesiadzinski, J. J. McMahon, C. J. Miller, B. Nord and L. Shaw, *The Astrophys. J.* **757**, 1 (2012).
117. D. E. Johnston, E. S. Sheldon, R. H. Wechsler, et al., arXiv://0709.1159 (2007).
118. E. Rozo, E. S. Rykoff, A. Evrard, et al., *The Astrophys. J.* **699**, 768 (2009).
119. N. Sehgal, G. Addison, N. Battaglia, et al., arXiv://1205.2369 (2012).
120. *Planck* Collaboration. III. *Astron. and Astrophys.* in press, arXiv://1204.2743 (2012).
121. N. Okabe, M. Takada, K. Umetsu, T. Futamase and G. P. Smith, *Pub. Astron. Soc. of Japan*, **62**, 811 (2010).
122. N. Okabe and K. Umetsu, *Pub. Astron. Soc. of Japan*, **60**, 345 (2008).
123. M. Kaplinghat, L. Knox and Y.-S. Song, *Phys. Rev. Lett.* **91**, 241301 (2003).
124. S. Wang, Z. Haiman, W. Hu, J. Khoury and M. May, *Phys. Rev. Lett.* **95**, 011302 (2005).
125. M. Shimon, S., Sadeh and Y. Rephaeli, *Mon. Not. R. Astron. Soc.* **412**, 1895 (2011).
126. Y. Rephaeli and M. Shimon, Proc. *Thirteenth Marcel Grossman Meeting on General Relativity*, edited by R.T. Jantzen, K. Rosquist and R. Ruffini (World Scientific, Singapore, 2014).
127. J. Tinker, et al., *The Astrophys. J.* **688**, 709 (2008).
128. S. M. Carroll, G. B. Field and R. Jackiw, *Phys. Rev. D* **41**, 1231 (1990).
129. S. M. Carroll and G. B. Field, *Phys. Rev. D* **43**, 3789 (1991).
130. S. M. Carroll, *Phys. Rev. Lett.*, **81**, 3067 (1998).
131. A. Lue, L. -M. Wang, M. Kamionkowski, *Phys. Rev. Lett.* **83**, 1506-1509 (1999).
132. S. Saito, K. Ichiki and A. Taruya, *J. Cosmology and Astrop. Physics* **0709**, 002 (2007).
133. L. Sorbo, *J. Cosmology and Astrop. Physics* **1106**, 003 (2011).
134. V. Gluscevic and M. Kamionkowski, *Phys. Rev. D* **81**, 123529 (2010).
135. A. Gruppuso, P. Natoli, N. Mandolesi, A. De Rosa, F. Finelli and F. Paci, *J. Cosmology and Astrop. Physics* **1202**, 023 (2012).
136. J. Kim and P. Naselsky, *Astrophys. J.* **714**, L265 (2010).
137. J. Kim and P. Naselsky, *Phys. Rev. D* **82**, 063002 (2010).
138. A. Gruppuso, F. Finelli, P. Natoli, F. Paci, P. Cabella, A. De Rosa and N. Mandolesi, *Mon. Not. R. Astron. Soc.* **411**, 1445 (2011).
139. P. K. Aluri and P. Jain, *Mon. Not. R. Astron. Soc.* **419**, 3378 (2012).
140. F. Paci, A. Gruppuso, F. Finelli, P. Cabella, A. De Rosa, N. Mandolesi and P. Natoli, *Mon. Not. R. Astron. Soc.* **407**, 399 (2010).
141. M. Zaldarriaga and U. Seljak, *Phys. Rev. D* **55**, 1830 (1997).
142. M. Zaldarriaga, *The Astrophys. J.* **503**, 1 (1998).
143. B. Feng, M. Li, J.-Q. Xia, X. Chen, X. Zhang, *Phys. Rev. Lett.* **96**, 221302 (2006).
144. P. Cabella, P. Natoli, J. Silk, *Phys.Rev. D* **76**, 123014 (2007).
145. B. Feng, H. Li, M. Li, X. Zhang, *Phys. Lett.* **B620**, 27 (2005).
146. E. Komatsu *et al.* [WMAP Collaboration], *Astrophys. J. Suppl.* **180**, 330-376 (2009).
147. E. Komatsu, et al. [WMAP Collaboration], *Astrophys. J. Suppl.* **192**, 18 (2011).
148. E. Y. S. Wu, et al., [QUaD Collaboration], *Phys. Rev. Lett.* **102**, 161302 (2009).
149. G. Gubitosi, L. Pagano, G. Amelino-Camelia, A. Melchiorri and A. Cooray, *J. Cosmology and Astrop. Physics* **8**, 21 (2009).
150. *Planck* Collaboration, The Scientific Programme of *Planck*, *ESA publication* ESA-SCI (2005)/1, arXiv://0604069 (2005).
151. G.-C. Liu, N. Sugiyama, A. J. Benson, C. G. Lacey, A. Nusser, *The Astrophys. J.* **561**, 504 (2001).
152. A. Cooray and D. Baumann, *Phys. Rev. D* **67**, 063505 (2003).
153. G. Lavaux, J. M. Diego, H. Mathias and J. Silk, *Mon. Not. R. Astron. Soc.* **347**, 729

(2004).
154. M. Shimon, Y. Rephaeli, B. W. 0'Shea and M. L. Norman, *Mon. Not. R. Astron. Soc.* **368**, 511 (2006).
155. U. Seljak and M. Zaldarriaga, *The Astrophys. J.* **469**, 437 (1996).
156. E. P. R. G. Ramos, A. J. C. da Silva and G.-C. Liu, *The Astrophys. J.*, **757**, 44 (2012).
157. D. J. Fixsen, E. S. Cheng, J. M. Gales, J. C. Mather, R. A. Shafer and E. L. Wright, *The Astrophys. J.* **473**, 576 (1996).
158. E. Komatsu, K. M. Smith, J. Dunkley, et al., *The Astrophys. J. Suppl.* **192**, 18 (2011).
159. R. Keisler, C. L. Reichardt, K. A. Aird, et al., *The Astrophys. J.* **743**, 28 (2011).
160. R. Hlozek, J. Dunkley, G. Addison, et al., *The Astrophys J.* **749**, 90 (2012).
161. J. Silk, *The Astrophys. J.* **151**, 459 (1968).
162. N. Kaiser, *Mon. Not. R. Astron. Soc.* **202**, 1169 (1983).
163. Y. B. Zel'dovich and R. A. Sunyaev, *Astrophys. and Space Science* **4**, 301 (1969).
164. C. Burigana, G. de Zotti and L. Danese, *Astron. and Astrophys.* **303**, 323 (1995).
165. R. Khatri and R. A. Sunyaev, J. Cosmol. Astropart. Phys. 9 (2012) 16.
166. P. McDonald, U. Seljak, S. Burles, et al., *The Astrophys. J. Suppl.* **163**, 80 (2006).
167. U. Seljak, A. Slosar and P. McDonald, *J. Cosmology and Astrop. Physics* **10**, 14 (2006).
168. A. Kogut, D. J. Fixsen, D. T. Chuss, et al., *J. Cosmology and Astrop. Physics* **7**, 25 (2011).
169. R. A. Sunyaev and Y. B. Zel'dovich, *Astrophys. and Space Science* **9**, 368 (1970).
170. R. A. Daly, *The Astrophys. J.* **371**, 14 (1991).
171. W. Hu, D. Scott and J. Silk, *The Astrophys. J. Lett.* **430**, L5 (1994).
172. J. Chluba, R. Khatri and R. A. Sunyaev, *Mon. Not. R. Astron. Soc.* **425**, 1129 (2012).
173. R. Khatri, R. A. Sunyaev and J. Chluba, *Astron. and Astrophys.* **543**, A136 (2012).
174. Y. B. Zel'dovich, A. F. Illarionov and R. A. Sunyaev, *Soviet Journal of Experimental and Theoretical Physics* **35**, 643 (1972).
175. A. F. Illarionov and R. A. Sunyaev, *Soviet Astronomy* **18**, 413 (1975).